Applied Catalysis B: Environmental 312 (2022) 121403

Contents lists available at ScienceDirect

Applied Catalysis B: Environmental

journal homepage: www.elsevier.com/locate/apcatb

# Hydrodeoxygenation of guaiacol *via in situ* $H_2$ generated through a water gas shift reaction over dispersed NiMoS catalysts from oil-soluble precursors: Tuning the selectivity towards cyclohexene

A.V. Vutolkina [a,*], I.G. Baigildin [a], A.P. Glotov [a,b], Al.A. Pimerzin [a,d], A.V. Akopyan [a], A.L. Maximov [a,c], E.A. Karakhanov [a]

[a] Lomonosov Moscow State University, GSP-1, 1–3 Leninskiye Gory, 119991 Moscow, Russia
[b] Gubkin Russian State University of Oil and Gas (NRU), 65 Leninsky Prospekt, 119991 Moscow, Russia
[c] A.V. Topchiev Institute of Petrochemical Synthesis, RAS, GSP-1, 29 Leninsky Prospekt, 119991 Moscow, Russia
[d] Samara State Technical University, 244 Molodogvardeyskaya Street, 443100 Samara, Russia

ARTICLE INFO

*Keywords:*
Unsupported NiMoS catalysts
Oil-soluble precursors
Guaiacol
Hydrodeoxygenation
Tunable selectivity to cyclohexene
*in situ* hydrogen generation
Water gas shift reaction

ABSTRACT

We report efficient hydrodeoxygenation of guaiacol *via in situ* hydrogen generated through Water Gas Shift (WGS) reaction over nanosized unsupported NiMoS catalysts with tunable selectivity toward cyclohexene. This strategy possesses a direct reaction route of oxygen-containing compounds from bio-oils depending on catalysts precursors and reaction conditions. The active catalytic species were formed *in situ* through the high-temperature decomposition of oil-soluble metal precursors followed by sulfidation in water-in-oil sulfur-containing emulsions. Unsupported NiMoS catalysts were found to provide 100% guaiacol conversion at 320–380 ℃ and 5 MPa CO pressure. Reaction routes and mechanisms for hydrodeoxygenation of guaiacol were proposed. Ni:Mo= 1:3 and sulfur content of 1.2–1.5 wt% favor higher cyclohexene selectivity decreases at low temperature and short reaction time (30–40 wt% water content, CO pressure of 5 MPa). The catalysts were found to be reusable at least 6 cycles in the sulfur-assisted hydrodeoxygenation of guaiacol with maintaining conversion, and active component evolution was studied.

## 1. Introduction

The development of effective technologies and catalysts for bio-oil upgrading became more important in the last few decades. The depletion of fossil fuels causes it decrease in the quality of petroleum feeds, whereas increasing the energy demand [1,2]. Therefore, the liquefaction of biomass yielded so-called “bio-oil” seems to be an attractive alternative to provide the rising energy demand, whereas saving fossil fuels and protecting thereof from depletion [2]. From this point, the non-food biomass, particularly lignocellulosic woodworking industry waste, is a good candidate for bio-fuel production [2–4]. As opposed to those from conventional crude oil, they have a high oxygen content (up to 60 wt% depending on biomass), which makes them inappropriate for use as motor fuels directly [4–6].

In fact, bio-oil is an acidic aqueous solution with a water content of up to 50 wt% [2,4,6]. The oxygen compounds like aldehydes, organic acids, ketones, furanes, phenolic compounds cause high acidity and corrosiveness, low stability and tendency to polymerize, high viscosity and low volatility, low heating value under combustion, and immiscibility with hydrocarbon fuels [6]. To improve the characteristics, the biomass-derived liquid products have to be upgraded, usually, through hydrotreatment, *i.e.* hydrodeoxygenation (HDO) processing, aimed at decreasing oxygen content and O/C ratio with that enhancing for C/H. The typical hydrotreatment catalysts contain transition metal sulfides (TMS) (Mo or W), supported on alumina. To enhance the activity, they are promoted by Ni or Co [7–9].

Usually, before being treated, the bio-oil has to be dehydrated for protecting TMS catalysts from deactivation [10]. The residual water from feed or formed during HDO poison the active phase by transforming thereof into inactive oxide species. At high temperatures, the water vapor destroys the support structure, resulting in the reorganization of the active component and decreasing activity [10].

The water-separation step is high-cost and energy-consuming. Meanwhile, being the major component of bio-oil, water may be

* Corresponding author.
*E-mail address:* annavutolkina@mail.ru (A.V. Vutolkina).

https://doi.org/10.1016/j.apcatb.2022.121403
Received 1 February 2022; Received in revised form 8 April 2022; Accepted 9 April 2022
Available online 14 April 2022

considered as a solvent for the selective hydrogenation of bio-oil-derived phenolic compounds to produce petrochemicals, *i.e.* cyclohexanol, cyclohexane, and cyclohexene [11,12]. This approach is based on polar effects when water allows targeted non-polar hydrocarbons separation. In this case, the selectivity to desirable products could be controlled by reaction medium modification or through the mass transfer constraints under biphasic conditions [11,12]. Thus, the development of efficient and resistant catalysts and novel approaches for water-assisted processing allows for enhancing bio-oil refining.

The second point for developing water-involved processes is that water can act as a source for *in situ* hydrogen generated through a water gas shift (WGS) reaction [13]. The processing of water-containing feed under WGS reaction conditions allows for withdrawing the water-separation step and conducting the single-stage processing to produce high-quality components of biofuels or bio-derived chemicals. Related to the bio-oil upgrading under WGS reaction conditions, two types of reaction (WGS and hydrotransformation of unsaturated and O-containing compounds) occurred, and TMS catalysts seem to be more appropriate. Being the major component of classic hydrotreatment catalysts, they also accelerate WGS reaction [14]. It provides effective transformation of reactants (*in situ* produced hydrogen and substrate) adsorbed on the neighboring active sites, excluding mass transfer influence [15]. Besides, these catalysts are more resistant to O-containing aromatics (e.c. phenolic derivatives acting as coke precursors) because of their regenerability under hydrogen sulfide [16].

The efficiency of TMS-based catalysts in hydrogen generation through a WGS reaction was shown experimentally and proved by density functional theory (DFT) calculations, which revealed the NiMo system as the most active [17,18]. This one-stage processing was applied for the upgrading of high viscous heavy oils [19]. The activation of water by CO yielded *in situ* hydrogen, which was involved in hydroupgrading, resulted in aromatics and sulfur content reduced. Many studies exhibited higher efficiency of hydrogenation with thus generated *in situ* hydrogen as compared to that for *ex situ* one [9,20–22]. To enhance the stability of supported sulfide catalysts to water vapor, the $TiO_2$-$Al_2O_3$, $ZrO_2$, $TiO_2$, Y-zeolite supports were used instead of alumina [13,14,17]. The activity and stability were found to be strongly depend on CO flow rate and water content. Moreover, the acidity of the carrier influences the interaction between the active component and support surface, and therefore dispersion and catalytic behavior [23]. It is difficult to balance these parameters to achieve the targeted conversion and selectivity for hydrogenation *via in situ* produced hydrogen.

In the scope of the destructive influence of water on the alumina-based catalysts, unsupported TMS ones are becoming more and more attractive. After the development of NEBULA and bulk catalysts with superior activity as compared to alumina-supported analogous, the dispersed catalysts were extensively studied for heavy oil, vacuum residue, and unconventional feed upgrading [24,25]. Advantageous, these catalysts may be formed *in situ* through high-temperature decomposition of water- or oil-soluble metal oxide precursors followed by sulfidation thereof to produce nanosized particles dispersed in the reaction media [9,22,26]. The water-soluble precursors are cheaper than oil-soluble analogous, but have a significant disadvantage. During decomposition at high temperature, the water evaporation is too fast, causing agglomeration of active species. It leads to low dispersion, and catalysts from water-soluble precursors have lower activity and stability as compared to their counterparts from metal-organic complexes. Opposite, the *in situ* synthesis from oil-soluble precursors is simple and reproducible. Due to better dispersion of metal-organic complexes in hydrocarbons, the resulted catalysts have smaller particle size with enhanced activity. In view of *in situ* formation of active species, the catalytic performance straightly depends on the oil-soluble properties of precursors, because it determines the dispersion of sulfide catalysts, and many attempts were made to develop new oil-soluble precursors with enhanced dispersibility [27,28]. By excluding mass transfer, diffusion limitation, and pore-plugging problems, when converting bulk molecules, dispersed catalysts were established as efficient and resistant systems for slurry phase hydroprocessing. Many works exhibited their applicability for hydroprocessing under WGS reaction conditions, e.c. for hydrodesulfurization, hydrodenitrogenation, and hydrogenation of aromatics [9,20,29]. The high activity in hydrodesulfurization of diesel fraction was reported for Mo sulfide catalysts obtained by dispersion of ammonium thiomolybdate in the hydrocarbon feed, containing 25 wt% of water [30]. We demonstrated the unsupported NiMo sulfide catalysts from water- and oil-soluble metal oxide precursors have superior activity and resistance to water in hydrogen sulfide-rich media as compared to alumina or mesoporous aluminosilicates, when converting naphthalene and benzothiophene derivatives under WGS reaction conditions [9,21,22,29,31]. In our previous studies, we thoroughly examined the relationship between hydrogen source (syngas/water or carbon monoxide/water) and efficiency of model feed hydrogenation depending on catalysts composition and structural properties, total pressure, temperature, and reaction time. The hydrogenation with *ex situ* hydrogen-rich media was found to be inhibited by water, whereas for CO-containing systems the conversion was comparable to that for water-free media.

When evaluating the catalytic behavior of sulfide unsupported catalysts in HDO, in most studies, the bio-derived phenolic compounds, *i.e.* guaiacol, are used as a model feed [32,33]. HDO of phenolic compounds over sulfide catalysts occurs at moderate temperatures (300–500 ℃) at a hydrogen pressure of 3–7 MPa. The higher the hydrogen pressure, the higher the selectivity to cycloalkanes, and the lower the oxygen content. The products of hydrotreatment of bio-oil-derived phenolic compounds include its O-containing derivatives, aromatics, or saturated cyclic hydrocarbons, and H/C *vs.* O/C ratio (exhibited as Van-Crevelen diagrams) determines the deep of oxygen removal and hydrogen saturation. The authors of [34] exhibited the efficiency of NiMo sulfide catalysts from water-soluble ammonium thiomolybdate and nickel nitrate in phenol HDO at 350 ℃ and 3 MPa. It was established that the increase in activity when promoted with Ni. Ni-promoted catalyst revealed the higher hydrogenation activity, and phenol transforms through hydrogenation pathway, where hydrogenation of aromatic ring occurs, followed by deoxygenation yielded hydrocarbons, *i.e.* cyclohexane. As for monometallic Mo sulfide, benzene forms with higher selectivity, indicating that the direct deoxygenation pathway (C-O bond scission followed by hydrogen saturation) is predominant. Meanwhile, increasing the Ni, the concentration of mixed Ni-Mo phase decreases, and higher content of bulk NiS leads to the catalyst activity decreases. A similar study proved the highest activity of an unsupported catalyst with Ni/Mo ratio of 0.3 in HDO of *p*-cresol at 275 ℃ and 4 MPa hydrogen pressure [35]. The higher the Ni content, the lower the catalytic activity, and cresol is becoming transformed through the hydrogenation route. When increasing temperature, the toluene selectivity increases, and the direct deoxygenation pathway becomes predominant. As it was found for unsupported catalysts, the NiS can provide the sites for hydrogen transfer. According to this hypothesis, the migration of active hydrogen from NiS to $MoS_2$, where it interacts with O-containing molecules, allows for enhancing activity. When the Ni content increases, the high concentration of NiS may lead to the anionic vacancies, where substrate molecules are adsorbed, decreases. The second point is the reduction of NiS to Ni metallic in the excess amount of hydrogen. It was also observed for 4-ethylphenol transformation over $NiS_2/MoS_2$ и $CoS_2/MoS_2$ catalysts at 275 ℃ and 4 MPa hydrogen pressure [36]. In another study, the CoMo and NiMo alumina-supported catalysts were synthesized by co-precipitation from water-soluble metal precursors to compare their activity in guaiacol HDO with that for unsupported analogous [37]. It was exhibited the higher activity of unsupported catalysts at 400 ℃ and 3 MPa hydrogen pressure with guaiacol conversion of 100% and 85% for NiMo and CoMo sulfide, respectively. For NiMo catalysts, the 55% selectivity to phenol was observed, whereas for CoMo the catechol forms as a predominant product with 40% selectivity. The authors underline the accessibility of the active site for bulk catalysts as compared to that

for alumina-supported counterparts, revealing 80–85% guaiacol conversion. The acidic support causes phenol transalkylation, and under recycling tests, these catalysts were shown to be destroyed by steam and deactivated due to enhanced coking.

Despite the numerous studies of bio-oil-derived phenolic compounds hydrodeoxygenation over unsupported sulfide catalysts, their catalytic behavior under WGS reaction conditions is not investigated yet. It is not thoroughly evaluated, how the CO pressure, temperature, water content, CO source (pure CO or syngas), CO/$H_2O$ ratio, catalysts composition, the acidity of the reaction solution affect the product distribution. Answering these fundamental questions would allow for the development of single-stage bio-oil processing to produce high-quality components of biofuels or bio-derived chemicals withdrawing energy-consuming and low-effective water-separation step.

We evaluated the HDO of guaiacol as a model platform of bio-oils *via in situ* hydrogen generated through WGS reaction over nanosized unsupported NiMo sulfide catalysts from oil-soluble precursors depending on the catalyst's and reaction media composition as well as reaction conditions. In an account of the transport phenomena considerations and solvent effect based on differences in solubility, we examined the influence of Ni promoter and content of sulfur, used as sulfiding agent precursor, on catalytic behavior in HDO of guaiacol and selectivity towards cyclohexene. We demonstrated the effectiveness of *in situ* hydrogen generation through the WGS reaction depending on water content and CO pressure compared to *ex situ* hydrogen and hydrogen-rich syn-gas media. It was shown the decrease of O/C with that increase for H/C under WGS reaction conditions, and the influence of CO pressure, water content, and CO/$H_2O$ ratio was established. Based on the product distribution at different temperatures and reaction times, we proposed the fundamental chemistry and reaction route for guaiacol transformation in the aqueous-phase HDO over unsupported NiMo sulfide catalysts and developed the approach for tuning the selectivity towards cyclohexene. Additionally, we examined the reusability and active phase evolution when recycling to show the stability during sulfur-assisted guaiacol transformation under WGS reaction conditions.

## 2. Experimental details

### 2.1. Chemicals

All chemicals were used without any further purification. Guaiacol (GUA) ($C_7H_8O_2$, ≥99%), molybdenum hexacarbonyl ($Mo(CO)_6$, 98%) were purchased from "Sigma-Aldrich". Toluene ($C_7H_8$, 99%), elemental sulfur (S, 98%), nickel naphthenate ($C_{22}H_{14}NiO_4$, 5–12%) were purchased from "Khimmed Chemical reactant" and "Alfa Aesar", respectively.

### 2.2. Characterization techniques

X-ray diffraction (XRD) was used to analyze the phase composition of the sulfide catalysts. The diffractograms were recorded in the 2θ range of $5^\circ - 75^\circ$ with a 0.05 step at a rate of $2^\circ * min^{-1}$ on the Bruker D2 PHASER device equipped with a monochromatic Cu Kα irradiation (λ = 0.154 nm). The stacking height was estimated according to the Debye–-Scherrer equation. The Rigaku PDXL software, with a powder database (ICSD standard files) was used for data interpretation. Thermo Scientific™ spectrometer Nicolet IR2000 equipped with multi-reflection HATR accessories were used to obtain Fourier-transform infrared (FT-IR) spectra. The spectra were recorded using a 45° ZnSe crystal in the range of 4000–500 $cm^{-1}$ with a resolution of 4 $cm^{-1}$. The transmission electron microscopy (TEM) images of unsupported sulfide catalysts were obtained on a JEOL JEM-2100 electron microscope operating at 200 kV and equipped with a $LaB_6$ gun and Olympus Quemesa 11 megapixel CCD camera. The samples were dispersed in ethanol using an ultrasonic bath and deposited on a Lacey TEM Cu grid (300 mesh, Ted Pella, Inc.). The structural characteristics of $MoS_2$ species were calculated from data obtained by handling black fringes over different areas of representative TEM micrographs. For this, Image-Pro Plus 7.0 software with standard drawing tools was used. The chemical composition and elemental maps were obtained on an EX-24065JGT energy dispersive X-ray (EDX) analyzer. EDX map for each sample was collected for 1 h. The X-ray photoelectron spectroscopy (XPS) measurements were performed at 20 °C on a KRATOS ES-300 spectrometer equipped with a hemispherical energy analyzer. Mg Kα ($h\nu = 1253.6$ eV, 170 W) was used as the photon source. The Au *4* $f_{7/2}$ (84.0 eV) and Cu *2*$p_{3/2}$ (932.7 eV) photoelectron lines were used for the binding energy (BE) scale calibration. The pass energy was set at 192 eV for the survey scan and 20 eV for the narrow scan. Due to the charging effects, the BE value for Mo*3d,* Ni*2p*, and S*2p* core-level spectra were calibrated by the C*1 s* = 284.6 eV or S*2*$p_{3/2}$ peak at 161.6 eV ascribed to the sulfide species. Before the deconvolution of the XPS profiles, the Gaussian-Lorentzian curves and Shirley background subtraction were applied to fit the spectra. The chemical state of the elements was identified by ascribing the BE of the peaks, and surface atomic concentrations were calculated by analyzing the individual spectral regions with the normalization of peak area ratios applying the corresponding atomic sensitivity factors.

### 2.3. Catalytic activity measurements

The hydrodeoxygenation (HDO) of guaiacol (GUA) was carried out in a stainless-steel batch reactor (50 $cm^3$) equipped with a magnetic stirrer. The unsupported catalysts were prepared *in situ* by high-temperature decomposition of oil-soluble metal precursors (nickel naphthenate and molybdenum hexacarbonyl) to produce metal oxide species followed by sulfidation. The elemental sulfur was used as a source of the sulfiding agent. In a typical experiment GUA (500 mg) and catalyst precursors ($C_{22}H_{14}NiO_4$– 17 mg, $Mo(CO)_6$ – 14 mg) were dissolved in toluene, suspended with elemental sulfur (30 −120 mg) under stirring, and transferred to the batch reactor. Afterward, the calculated amount of distilled water (0.5 – 2.0 ml) was added resulting in a water-in-oil emulsion. The water content was calculated in an account of ensuring desirable CO:$H_2O$ molar ratio. The total mass of the reaction mixture was 5 g. The portions of the precursors and reagents were calculated to ensure the Mo:Ni molar ratio of 3:1 and the GUA:Mo molar ratio of 75:1. Reactor was sealed with the reactant gases (carbon monoxide, hydrogen, or syngas) under the initial pressure (3.0 – 7.0 MPa at room temperature) and leak tested. Next, the reactor was heated gradually (25 °C/min ramp) to a designated temperature (320 – 380 ℃) with a stirring speed of 700 rpm in a thermostatically controlled oven. The reaction was terminated after 4–8 h at the designated temperature. After the reaction was completed, the reactor was cooled to room temperature and disassembled. The liquid products were decanted, and the catalyst was filtered and centrifugated. The resulting dark powder was washed with toluene and dried in an inert atmosphere. Blank tests of HDO were performed in similar reaction conditions without catalyst and sulfur, which presented negligible guaiacol conversion (<1%).

Liquid products were analyzed on Crystal 4000 M gas chromatograph (CHROMATEC SDO JSC), equipped with a flame ionization detector and capillary column PetrocolTM (Supelco 0.25mmx50m). The individual components were identified by GC–GC-TOF MS analysis on LECO Pegasus chromatograph equipped with Rxi-5Sil (0,1mmx1,7 m) and Rxi-17Sil (0,25mmx30m) capillary columns. Phenol (PHE), catechol (CAT), cyclohexanone (CH-one), cyclohexene (CH-ene), and cyclohexane (CH-ane) were identified as the main products of guaiacol hydrodeoxygenation. The oxygen-containing products of PHE alkylation with CH-ene were named oxygenates (Oxy), whereas its hydrogen saturated derivatives were ascribed to hydrocarbons (HC). GUA conversion, product selectivity, H/C, and O/C ratios for Van-Crevelen diagrams were calculated using the following equations:

$$Conversion = \frac{\Sigma S_p \quad \times 100\%}{\Sigma S_p + S_{GUA}} \tag{1}$$

$$Selectivity = \frac{S_i \quad \times 100\%}{\Sigma S_p} \tag{2}$$

$$\frac{H}{C} = \frac{\left(Sel_{PHE} * 1 + Sel_{Me-PHE} * \frac{8}{7} + Sel_{CAT} * 1 + Sel_{CH-one} * 2 + Sel_{CH-ene} * \frac{10}{6} + Sel_{CH-ane} * 2 + Sel_{HC} * \frac{16}{12} + Sel_{Oxy} * \frac{16}{12} + Sel_{GUA} * \frac{8}{7}\right)}{100} \tag{3}$$

$$\frac{O}{C} = \frac{\left(Sel_{PHE} * \frac{1}{6} + Sel_{Me-PHE} * \frac{1}{7} + Sel_{CAT} * \frac{3}{7} + Sel_{CH-one} * \frac{1}{6} + Sel_{Oxygenates} * \frac{1}{12} + Sel_{GUA} * \frac{2}{7}\right)}{100} \tag{4}$$

where $S_p$ – peak area of products and $S_{GUA}$ – peak area of guaiacol, $S_i$ – peak area of *i*-product, $Sel_i$ – selectivity toward *i*-product.

The characteristics of sulfide species and the composition of sulfide catalysts were calculated as follows [38,39]:

$$D = \frac{(Mo_e + Mo_c)}{Mo_T} = \frac{(6 * n_i - 12) * \overline{N} + 6 * \overline{N}}{(3 * n_i^2 - 3 * n_i + 1) * \overline{N}} = \frac{6 * n_i - 6}{3 * n_i^2 - 3 * n_i + 1} \tag{5}$$

$$w_{NiMoS} = \frac{[NiMoS] * w_{Ni}}{100} \tag{6}$$

$$w_{NiS} = \frac{[NiS] * w_{Ni}}{100} \tag{7}$$

$$w_{MoS_2} = \frac{[MoS_2] * w_{Mo}}{100} \tag{8}$$

$$p\left(\frac{Ni}{Mo}\right)_s = \frac{c_{NiMoS}}{c_{MoS_2}} \tag{9}$$

$$p(Ni/Mo)_e = \frac{p(Ni/Mo)_s}{Mo_e + Mo_c} * Mo_T = \frac{p\left(\frac{Ni}{Mo}\right)_s}{D} \tag{10}$$

where $D$ – the dispersion of active component; $Mo_e$, $Mo_c$ – the total number of Mo atoms at the edge and corner sites of $MoS_2$, respectively; $Mo_T$ – the total number of Mo atoms; $\overline{N}$ – the average stacking number; $n_i$ – the total number of Mo atoms along one side of the $MoS_2$ slab; $w_{NiMoS}$, $w_{NiS}$, $w_{MoS2}$– the effective Ni content in NiMoS, NiS, and Mo in $MoS_2$ phase, respectively; *[NiMoS], [NiS], [$MoS_2$]* – relative concentration of NiMoS, NiS, and $MoS_2$ phase, respectively (%); *ωNi, ωMo* – effective Ni and Mo concentration, respectively (wt%); $p(Ni/Mo)_s$ – Ni promotion of $MoS_2$ slab; $p(Ni/Mo)_e$ – Ni/Mo atomic ratio on the edges; $c_{NiMoS}$– absolute concentration of Ni in NiMoS species (at%); $c_{MoS2}$– absolute concentration of Mo in $MoS_2$ phase (at%).

## 3. Results and discussion

### 3.1. Effect of Ni promoter on the guaiacol transformation under water gas shift reaction conditions

Independently from catalysts composition, **GUA** conversion reaches > 99% and **PHE** was found to be the major product with 45–47% selectivity for non-promoted Mo-based catalyst and its counterpart with Ni:Mo molar ratio of 1:1 (Fig. 1**A**). The higher the Mo content, the lower the **PHE** selectivity, minimized at Ni:Mo= 1:3 and Ni:Mo= 1:4 (40% for both cases). Opposed to the Ni:Mo ratio of 1:3, where the **CH-ene** content reaches 28%, for all the other cases **CAT** was detected as one of the predominant products with 13–19% selectivity decreasing in the following trend: Ni:Mo= 1:2 > Ni:Mo= 1:4~Ni:Mo= 1:1 >Mo.

Since the solubility of **CAT** in water, the high selectivity toward **CAT** results from the water-rich reaction media. It causes by the lower activity of these catalytic compositions in WGS as compared to that for Ni:Mo molar ratio of 1:3. Therefore, the stagnant water layer covering the

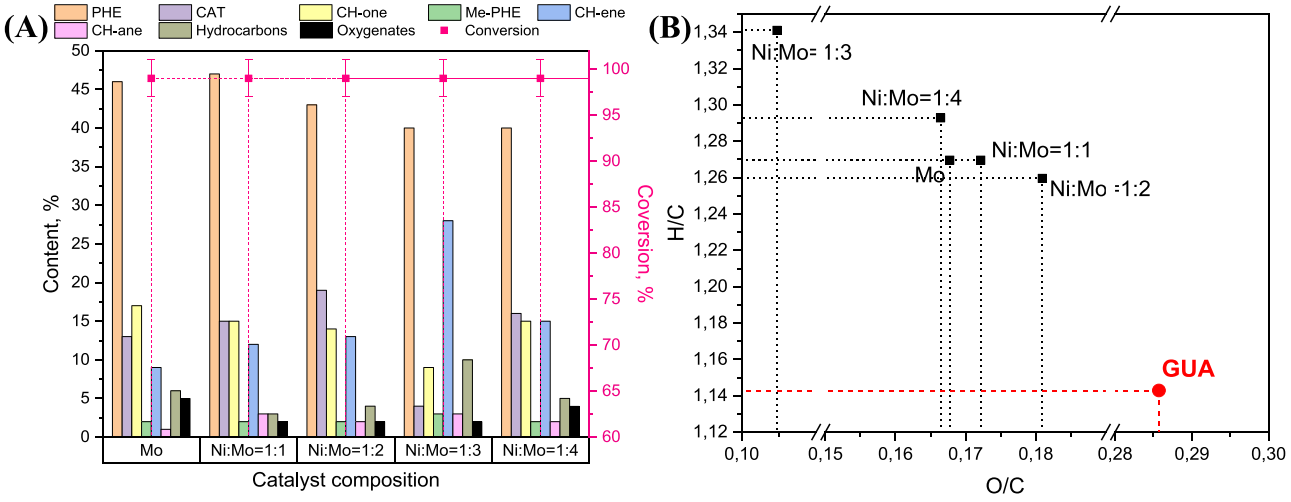


**Fig. 1.** (A) Products distribution and (B) Van-Crevelen diagram for products of GUA transformation under WGS reaction conditions depending on the catalytic composition. *Reaction conditions:* T = 360 °C, t = 6 h, ω(Mo) = 0.10 wt%, ω(S) = 1.25 wt%, p(CO) = 5 MPa, ω($H_2O$) = 20 wt%, CO:$H_2O$ = 1.8 (mol/mol).

catalyst active species may form. It disfavors **CH-ene** desorption because of its low solubility in water and at a short reaction time the **CH-ene** may be involved in condensation with **PHE** yielded cyclohexylphenol, which may undergo further hydrogenation/dehydration to bicyclohexanol or corresponding hydrocarbons like phenylcyclohexane and bicyclohexyl. **CAT** converted into **CH-one** followed by its hydrogenation/dehydration to **CH-ene**. Aside from catalyst composition with Ni:Mo molar ratio of 1:3, where **CH-one** selectivity is not higher than 9%, for all the other counterparts the content of **CH-one** is comparable and achieves 14–17%. The total yield of cresols (products of PHE alkylation with methanol) and **CH-ane** was not higher than 5%.

According to the widely acknowledged "rim-edge" model proposed by Topsøe and coworkers, the higher activity of promoted catalysts deals with Ni donating the electrons, weakening the metal–sulfur bond [40]. It leads to increasing the amount of labile sulfur and therefore enhancing the formation of coordinatively unsaturated sites (CUS) on the edges of $MoS_2$ slabs because of easier $H_2S$ elimination, which is more favorable on the metallic edge as compared to sulfur ones [41]. Due to the Ni having a greater affinity for metallic edges, the decoration of Mo-edges of $MoS_2$ slabs with Ni leads to increasing the amount of CUS, where the flat sorption of aromatic rings occurred [42,43]. It leads to an enhanced hydrogenation activity with a higher reactions rate [44]. Therefore, for unpromoted Mo-based sulfide catalysts despite the high **GUA** conversion, the yield of more saturated or dehydrated products is lower than for Ni-containing counterparts with Ni:Mo ratios of 1:3 and 1:4, which is reflected as the O/C and H/C molar ratios (Fig. 1**B**). Meanwhile, the comparable activity of unpromoted Mo-based catalysts with those for Ni-containing ones (Ni:Mo=1:1 and Ni:Mo=1:2) causes by the impact of "rim" sites on the basal plane of the $MoS_2$. For unsupported catalysts, these sites may provide adsorption of substrates through van der Waals interactions, increasing the conversion of **GUA** and intermediates [43]. Due to the hydroconversion of O-containing aromatic compounds is expected to be controlled by the number and nature of promoter decorated the Mo-edge, the second point is Ni content. As reported for Ni-promoted Mo sulfide catalyst, when increasing Ni content up to Ni/Mo ratio of 0.15 the Ni predominantly incorporates to Mo edge forming NiMoS phase [44]. After that, the S edges are decorated with Ni, whereas the amount of Ni-promoted Mo edges decreases. Therefore, the higher the Ni/Mo ratio, the lower the average number of Mo- and S-edge mixed Ni-Mo sites normalized per molybdenum atom in the nanocrystallites [44]. Further introduction of promoter doesn't contribute any more to the decoration of $MoS_2$ nanocrystallites and high Ni content may lead to segregated $Ni_xS_y$ phases, which exhibited much worse activity compared to the NiMoS phase [45]. As reported, an optimal Ni:Mo ratio is 1:3, which is in full accordance with the results of catalytic testing. When the Ni content is too low, the decoration of Mo-edges with Ni and, as a consequence, the amount of CUS formed through $H_2S$ elimination from metallic edges decreases, negatively influencing the rate of **GUA** and intermediates transformation.

### 3.2. *Effect of sulfur content on the guaiacol transformation under water gas shift reaction conditions*

To the best of our knowledge, the sulfide catalysts deactivate when contacting with water due to reorganizing of the active component [10]. Therefore, for the regeneration of active sites, the sulfur additive was applied [16,46]. We used elemental sulfur as a sulfiding agent precursor. At high temperatures, the sulfur interacts with hydrogen *in situ* generated through a WGS reaction to form hydrogen sulfide. When decomposing the oil-soluble salts yielded metal oxide, $H_2S$ acts as a sulfiding agent, allowing for *in situ* formations of active sulfide species. During the reaction that occurred in water-rich media sulfur additive also favors active phase regeneration. $H_2S$ also affects the number of active sites. According to the widely acknowledges mechanism, $H_2S$ is dissociatively adsorbed on the Lewis acid sites forming CUS, where substrate molecules are adsorbed and transformed [40,41]. When the low content of hydrogen sulfide, the number of CUS and regenerability of the active sulfide component decrease. It results in lower **GUA** conversion and a higher O/C ratio (Fig. 2).

On rising the sulfur content to 1.2 and 1.5 wt%, the yield of **CH-ene** increases, whereas that for **CH-one** decreases. The higher content of sulfur favors **CH-one** dehydration due to the higher concentration of hydronium ions from hydrogen sulfide, which may dissolve in water. It also affects on alkylation of **PHE** with **CH-ene** yielded oxygenates and hydrocarbons. Enhanced acidic properties of catalysts with 1.2 and 1.5 wt% of sulfur additive are proved by the higher content of **Me-PHE** formed through the alkylation of **PHE** with methanol. The selectivity to **PHE** remains unchanged, whereas the content of **CAT** decreases with sulfur additive. It means that sulfur enhances catalytic activity through the formation of active sites available for WGS reaction producing *in situ* hydrogen and hydrogenation of **CAT** to **CH-one**.

When increasing the sulfur content up to 2.5 wt%, **GUA** conversion remains unchanged, whereas the O/C ratio increases and H/C ratio decreases significantly as compared to those for 1.2–1.5 wt% (Fig. 2). Similar to low sulfur content, the products contain a high amount of **PHE** and **CAT**, indicating the inhibiting effect of sulfur excess. It may be

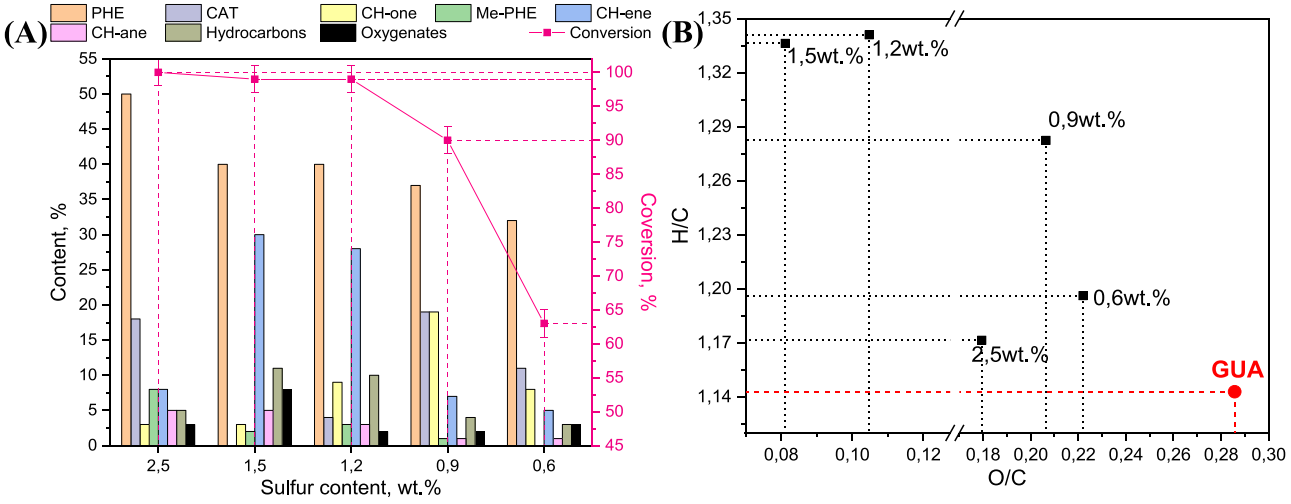


**Fig. 2.** (A) The influence of weighted sulfur content on the activity of Ni-Mo sulfide catalyst from oil-soluble metal precursors in GUA transformation under WGS reaction conditions and (B) Van-Crevelen diagram for products of GUA hydrodeoxygenation. *Reaction conditions:* T = 340 °C, t = 6 h, ω(Mo) = 0.10 wt%, Ni:Mo= 1:3 (mol/mol), p(CO) = 5 MPa, ω($H_2O$) = 20 wt%, CO:$H_2O$ = 1.8 (mol/mol).

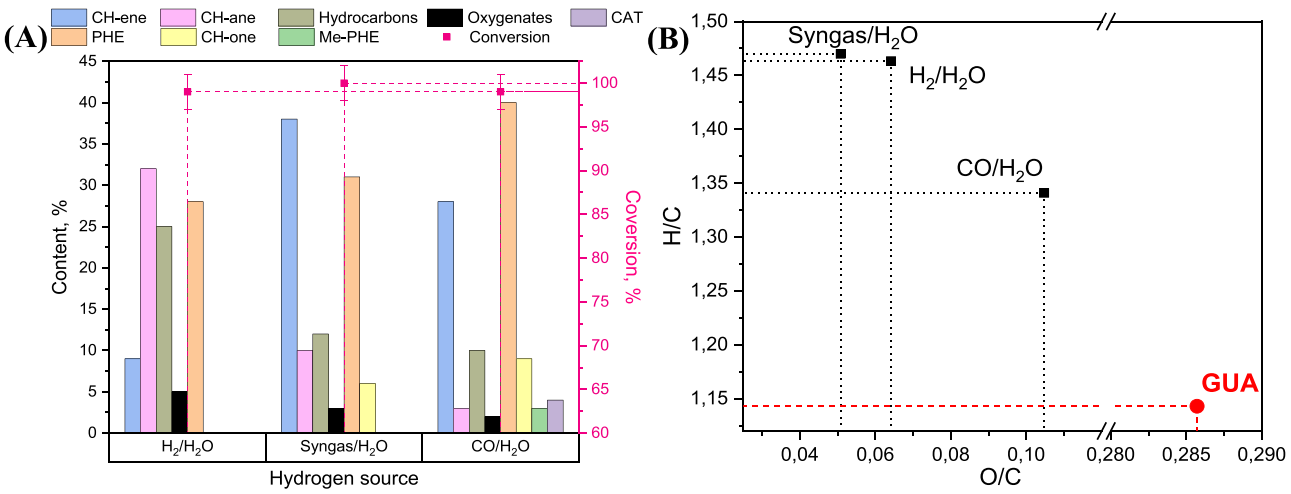


**Fig. 3.** *Reaction conditions:* T = 340 °C, t = 6 h, ω(Mo) = 0.10 wt%, ω(S) = 1.25 wt%, Ni:Mo= 1:3 (mol/mol), p = 5 MPa; for syngas/$H_2O$ and CO/$H_2O$ systems: ω($H_2O$) = 20 wt%, CO:$H_2O$ = 1.8 (mol/mol).
(A) The influence of hydrogen source on GUA transformation over Ni-Mo sulfide catalyst from oil-soluble metal precursors under WGS reaction conditions and (B) Van-Crevelen diagram for products of GUA hydrodeoxygenation.

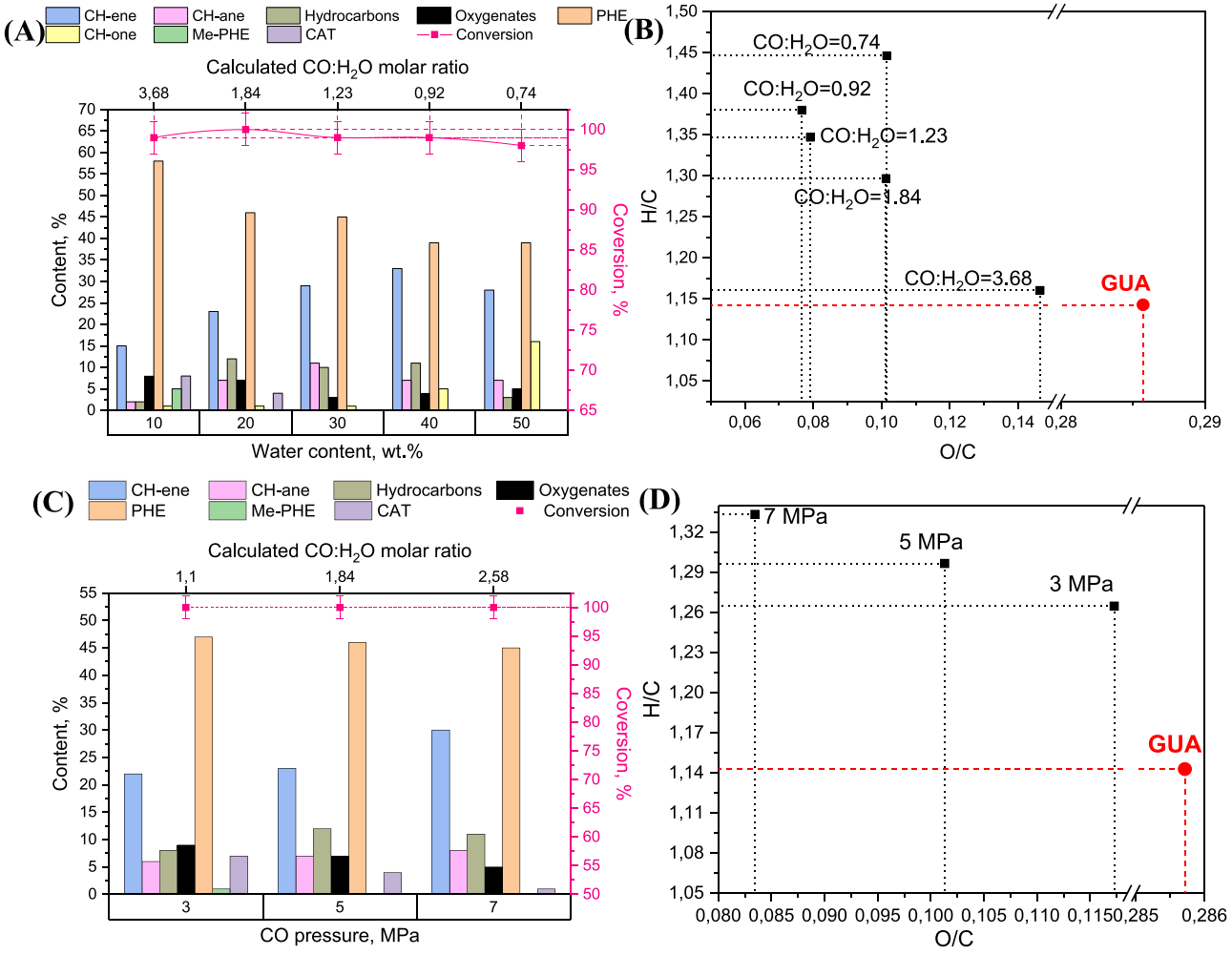


**Fig. 4.** The influence of (A) water content and (C) CO pressure within CO/$H_2O$ molar ratio on GUA transformation over Ni-Mo sulfide catalysts from oil-soluble metal precursors under WGS reaction conditions and (B, D) Van-Crevelen diagram for products of GUA hydrodeoxygenation. *Reaction conditions:* T = 360 °C, t = 6 h, ω(Mo) = 0.10 wt%, ω(S) = 1.25 wt%, Ni:Mo= 1:3 (mol/mol); for (A, B): p (CO) = 5 MPa; for (C, D): ω($H_2O$) = 20 wt%.

caused by the high hydrogen sulfide concentration, which negatively affects the amount of CUS on $MoS_2$ edges [47]. The $H_2S$ concentration influences the shape of $MoS_2$ crystallines: at high content of $H_2S$ in the gas phase, the active component is triangular, whereas low $H_2S$ concentration favors a hexagonal shape [15]. This high sulfur content leads to an increase the acidity [42], reflected in increasing dehydration of **CH-one** and **PHE** alkylation with methanol and **CH-ene**. Therefore, at 2.5 wt% of sulfur, the high O/C ratio is accompanied by insufficient hydrogenation, which is expressed in a low H/C ratio.

### *3.3. Effectiveness of guaiacol transformation via hydrogen in situ generated through a water gas shift reaction as compared to that for hydrogen-rich gaseous media*

Since hydrogen is involved in $H_2S$ production and transformation of GUA under WGS reaction conditions, *i.e.* in water-containing reaction media, we evaluate the influence of hydrogen sources on GUA conversion and product selectivity. Independently from the hydrogen source, GUA conversion reaches > 99% (Fig. 3**A**). As expected, despite the inhibiting effect of water, hydrogen-containing gas mixture favors faster active sulfide species formation and therefore effective transformation of phenolic compounds to corresponding hydrocarbons. For $H_2/H_2O$ system reaction products contain 66% of hydrocarbons with 25% of **CH-**

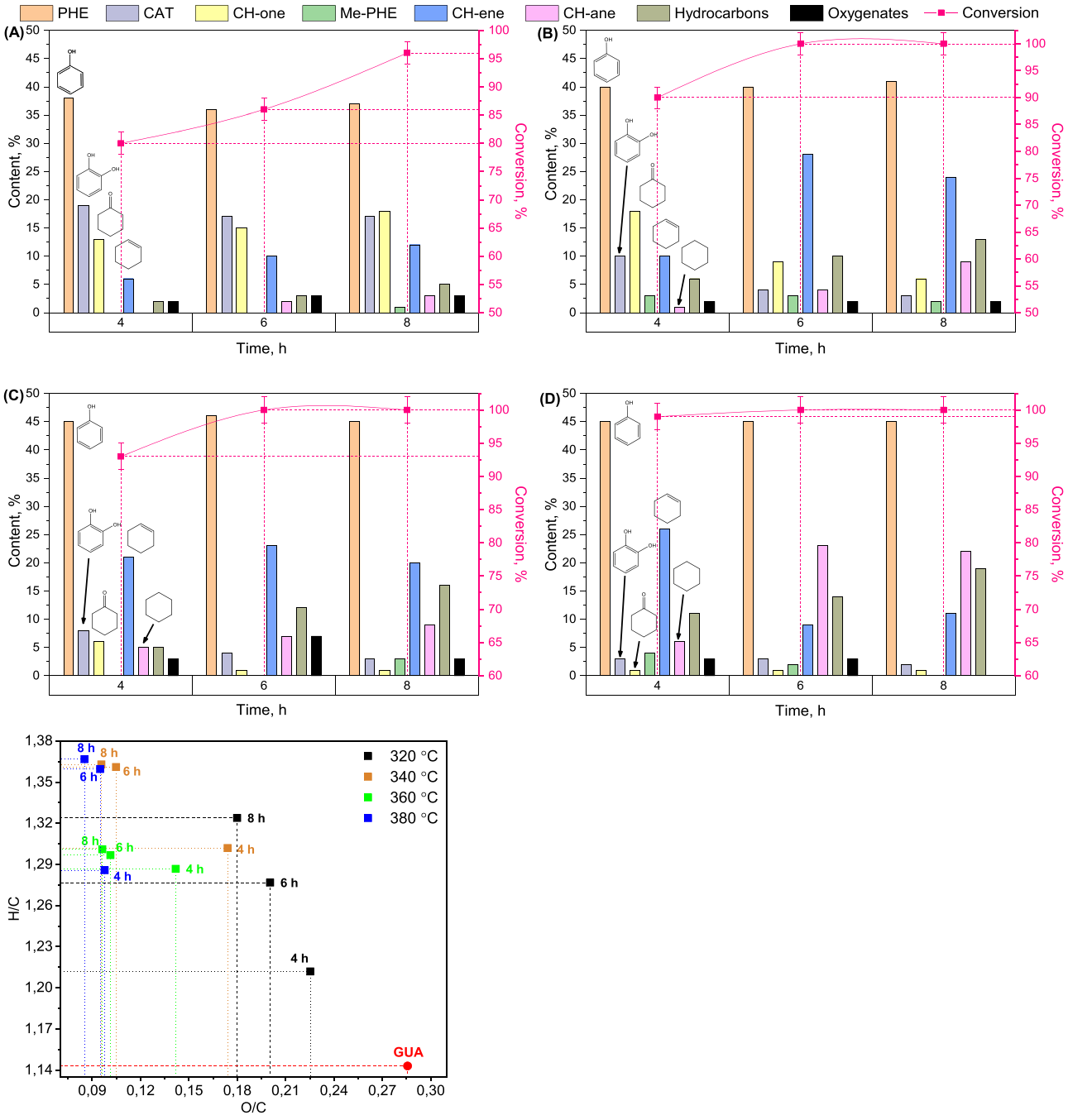


**Fig. 5.** (A-D) Product distribution of GUA transformation over Ni-Mo sulfide catalyst from oil-soluble metal precursors under WGS reaction conditions at (A) 320 ℃, (B) 340 ℃, (C) 360 ℃, and (D) 380 ℃; (E) temperature and time-dependent Van-Crevelen diagram for products of GUA hydrodeoxygenation. *Reaction conditions:* ω(Mo) = 0.10 wt%, ω(S) = 1.25 wt%, Ni:Mo= 1:3 (mol/mol), ω(S) = 1.3 wt%, ω($H_2O$) = 20 wt%, p(CO) = 5 MPa (at 25 ℃), CO:$H_2O$ = 1.8 (mol/mol).

**ane**, whereas the content of oxygenated compounds like **PHE** and its derivatives (resulted from alkylation of PHE with CH-ene) is only 33%. In syngas/$H_2O$ system **CH-ene** becomes a predominant product with 38% selectivity due to $MoS_2$ acting as active sites for WGS reaction, where the CO sorption occurs. Based on the product distribution, one may conclude that GUA rapidly transforms into **CH-ene**, which involved to alkylation of **PHE** or hydrogenated to **CH-ane** as the water content decreases. For the non-hydrogen CO/$H_2O$ system, the highest **PHE** selectivity was observed, and lower hydrogen-saturated but higher oxygen-containing products were yielded (Fig. 3**B**). Aside from two others, in CO/$H_2O$ system, where simultaneous hydrogen generation and GUA transformation occurred, intermediate **CAT** was detected in the products, indicating the lower reaction rate of **CAT** hydrogenation to **CH-one** in the lack of hydrogen. It is also proved by decreasing of **CH-ene** content, whereas comparable selectivity to oxygenates and hydrocarbons with that for syngas/$H_2O$ medium. For the latter one, the highest H/C molar ratio and deoxygenation degree as compared to those for the two other systems was achieved, indicating the positive impact of WGS reaction on total hydrogen content.

### 3.4. Effect of water content and CO pressure on the guaiacol transformation under water gas shift reaction conditions

Since under WGS reaction conditions product distribution of GUA transformation depends on the effectiveness of hydrogen generation, we have evaluated the influence of water content and CO pressure as the parameters affect the equilibrium for that reversible reaction. As depicted in Fig. 4**A, C**, the GUA conversion reaches > 99% independently from water content and CO pressure. Meanwhile, at the constant CO pressure of 5 MPa the content of **PHE** decreases, whereas that for **CH-ene** increases followed by decreasing with water. The same trend was observed for **CH-ane**. Obviously, when containing 10 wt% of water, the system is lacking hydrogen, which is proved by intermediate **CAT** formation decreasing to 0 at 20 wt% of water. **CH-ene** and **CH-ane** were detected in a trace amount, whereas the content of **PHE and** its derivatives reaches 44%. It leads to a low H/C molar ratio with high oxygen content (Fig. 4**B**). Starting from 20 wt% and up to 40 wt% water O/C molar ratio decreases, whereas that for H/C increases. It results from a higher **CH-ene, CH-ane,** and hydrocarbons yield, which shows sufficient hydrogen formation. Notably, the yield of hydrocarbons maintains almost constant over the range of mass water content of 20–40%. The highest selectivity toward **CH-ane** (11%) achieves for 30 wt% of water. Despite the highest **CH-ene** content, at 40 wt% the yield of **CH-one** increases, whereas that for **CH-ane** decreases. When containing 50 wt% of water, the inhibiting effect was observed: selectivity toward **CH-one** reaches 16% with **CH-ene** and hydrocarbons decreasing. Concluded, the 20–40 wt% of water corresponded to CO:$H_2O$ molar ratio of 1.8–0.9 is optimal for achieving the deep hydrogenation-deoxygenation degree.

As for the CO pressure, it influences insignificantly compared with water content. Thus, when the water content was fixed at 20 wt%, the H/C ratio increases, whereas O/C decreases with CO pressure (Fig. 4**D**). It is provided by lower **CAT** and oxygenates content with higher **CH-ene** and hydrocarbons yield. Note, that selectivity toward **PHE** maintains almost constant over the whole CO pressure range. At CO pressure of 3 MPa, which is equal to the calculated CO:$H_2O$ molar ratio of 1.1, the H/C ratio is lower as compared to that achieved by varied water content (1.34–1.38 *vs.* 1.26). It becomes more significant for O/C ratio: 0.08 *vs.* 0.11 for CO:$H_2O$ molar ratio of 0.92–1.23 (water content of 40 and 30 wt% at CO pressure of 5 MPa) and 1.1 (CO pressure of 3 MPa with a water content of 20 wt%), respectively. Opposed to that, the higher CO pressure of 7 MPa (calculated CO:$H_2O$ molar ratio of 2.58) favors the deeper hydrogenation and deoxygenation degree (H/C=1.33, O/C=0.08) compared with that for CO:$H_2O$ molar ratio of 1.84 (H/C=1.30, O/C=0.10).

### 3.5. Effect of temperature and reaction time on the guaiacol transformation under water gas shift reaction conditions

The temperature-dependent transformation of GUA revealed the simultaneous dehydroxylation and demethylation yielded **PHE** and **CAT**, respectively (Fig. 5). At 320 ℃ PHE, **CAT** and **CH-one** are predominant products, and the content of **CH-ene** increases with time. According to the product distribution the higher the temperature, the faster the **GUA** transforms to **PHE**, which is indicated by the **PHE** content increases from 37%–40% at 320–340 ℃ to 45% at 360 ℃, and that maintains constant even at 380 ℃ over the whole reaction time. Starting from 340 ℃, **CH-ene** increases, followed by decreasing with time. It is caused by **CH-ene** hydrogenation yielded **CH-ane** with 22–23% selectivity at 380 ℃ for 6–8 h. Based on the product distribution, we have concluded that at 320 ℃ the rate of WGS reaction is lower, which leads to lacking hydrogen. It results in a high O/C ratio (Fig. 5**E**).

*In situ* accumulation of hydrogen with time causes the increase of H/C ratio. Note that at 320 ℃ the total content of hydrocarbons and oxygenates maintains almost constant independently from reaction time (Fig. 5**A**). It shows that alkylation of **PHE** with **CH-ene** occurs insignificantly despite water influence. Temperature increasing to 340 ℃ accelerates the accumulation of hydrogen produced *in situ* through the WGS reaction. Therefore, the **PHE** and **CAT** content decreases, whereas that for **CH-one** and **CH-ene** increases, and **CH-ene** selectivity reaches 28% for 6 h. Higher temperature favors **PHE** alkylation. Aside from supported catalysts, where the support acidic and structural properties favour alkylation of **PHE** and **GUA** with methanol forming cresols and veratrole, respectively [48], for unsupported analogous **Me-PHE** was detected in a trace amount (Fig. 5**B-D**).

Meanwhile, the total content of dimers increases at 6 h afterward maintains unchanged. It means that alkylation of **PHE** with **CH-ene** predominantly occurs until the reaction media contains water. When the water is fully involved in WGS reaction, the hydrogen partial pressure increases, leading to the hydrogenation of **CH-ene** to **CH-ane** and oxygenates to hydrocarbons. These products of **GUA** become predominant at 360–380 ℃ for 6–8 h. Therefore, despite the higher **PHE** yield (of *ca.* 45%), the O/C ratio is lower as compared to that for 320–340 ℃, where the **PHE** content is 5–10% lower. At 340 ℃ the rate of **GUA** demetoxylation is lower, but this temperature is sufficient for effective *in situ* hydrogen generation through the WGS reaction. Thus, starting from 6 h the **CAT** and **CH-one** content decreases with that increasing for **CH-ene**. It results in H/C and O/C ratios becoming comparable with those for 380 ℃. As clearly seen from Fig. 5**E**, the lower the temperature, the more noticeable the reaction time on C/O ratio, whereas at 380 ℃ the reaction time enables to achieve the higher H/C ratio.

### 3.6. Reaction pathway for guaiacol transformation under water gas shift reaction conditions and key parameters for tuning the selectivity towards cyclohexene

Based on the influences of catalysts' composition and reaction parameters on products, we proposed the reaction pathway for **GUA** transformation in water-containing media over unsupported Ni-Mo sulfide catalysts under WGS reaction conditions (Scheme 1).

HDO of guaiacol (**GUA**) starts from its direct demetoxylation to phenol (**PHE**) or demethylation resulted in catechol (**CAT**). Supposedly, **GUA** aromatic ring may be hydrogenated to 2-methoxycyclohexanone intermediate, which rapidly transforms to cyclohexanone (**CH-one**) *via* two reaction pathways. The first one is hydrogenation and non-acid catalyzed hydrolysis of the methoxy group with further alcohol dehydration and hydrogenation of cyclohexenone. The other one is hydrogenation, acid-catalyzed hydrolysis to diol, followed by dehydration and ketone/enol isomerization. As reported, these steps are very fast, so that intermediate products were not detected [32,49,50]. **CAT** may undergo dehydration to **PHE** and, which is more likely, hydrogenation to cyclohexane diol through 2-hydroxycyclohexanone intermediate. The

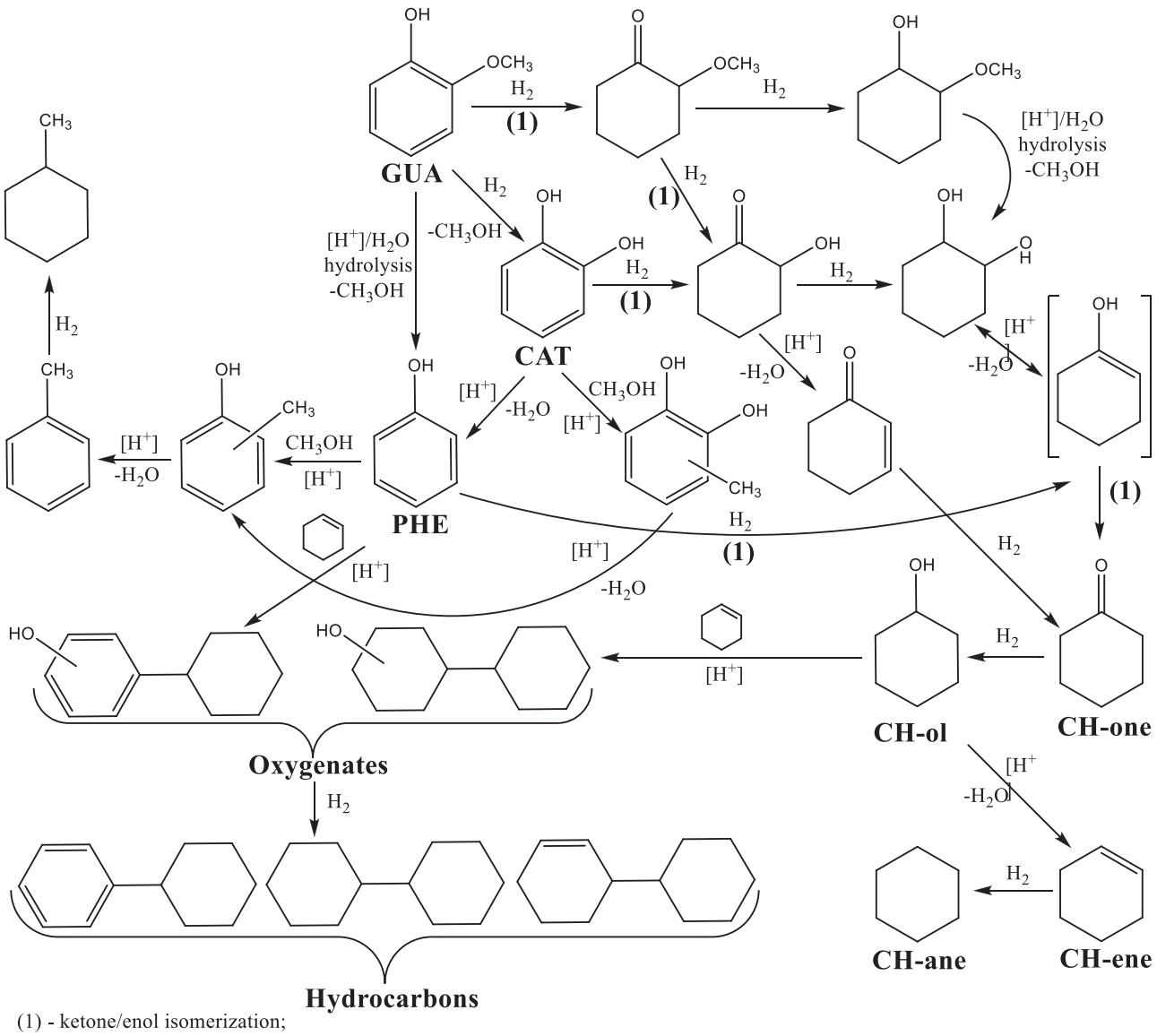


**Scheme 1.** Reaction pathways for HDO of guaiacol in water-containing media over unsupported Ni-Mo sulfide catalysts under WGS reaction conditions.

latter transforms into **CH-one** *via* two parallel routes: alcohol dehydration and ketone/enol isomerization (major pathway) or alcohol dehydration and alkene hydrogenation (minor pathway). It explains the **CH-one** as a dominant reaction product. It should be not to rule out that **CAT** may convert through the hydrogenation of only one double bond followed by acid-catalyzed dehydration of the resulted diol to **PHE**, which hydrogenated to **CH-one**. Hydrogenation of **CH-one** results in cyclohexanol (**CH-ol**) followed by its dehydration to cyclohexene (**CH-ene**). The latter may form through the direct hydrogenation/dehydration of **CH-one**. **CH-ene** is saturated by hydrogen to cyclohexane (**CH-ane**) or can be involved in the alkylation of **PHE** yielded corresponding oxygenate (cyclohexylphenol). If the hydrogen

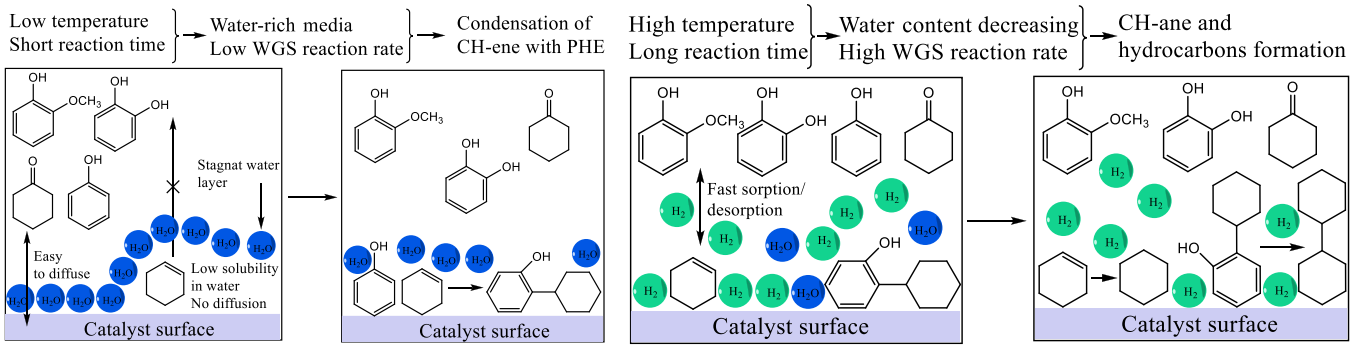


**Scheme 2.** Schematic representation of reaction conditions, influencing products and selectivity.

pressure is enough, aromatic ring saturation leads to bicyclohexanol, followed by its dehydration forming bicyclohexyl or corresponding alkene. Supposedly, the direct deoxygenation (DDO) of phenylcyclohexanol also occurs, because a trace amount of phenyl cyclohexane was detected.

As for **PHE** transformation, due to the high C-O bond energy for $C_{Ar}$ – OH (414 kJ $mol^{-1}$) [49], the direct deoxygenation (DDO) of PHE to benzene doesn't occur. Supposedly, PHE aromatic rings undergo hydrogenation forming cyclohexenol as an intermediate, which transforms to **CH-one** during ketone/enol isomerization.

According to the product distribution, **PHE**, **CAT**, **CH-one,** and **CH-ane** are predominant. Products of **PHE** and **CAT** alkylation with methanol were not observed. As it was reported, **CH-one** is a stable intermediate, while in the presence of acid catalysts at high hydrogen pressure and temperature, the main product obtained is **CH-ol.**

High selectivity to **CH-one** may be caused by its stabilization on the weak Lewis acid sites of $MoS_2$ [12]. The formation of **CH-ene** is due to the influence of hydrogen sulfide, which may dissolve in water, and being acid decrease pH [42]. The higher hydronium ion concentration in the reaction media and sufficiently high reaction temperature lead to the dehydration of **CH-one** or **CH-ol** to **CH-ene**. Interestingly, that further hydrogenation of **CH-ene** to **CH-ane** is inhibited under low temperature or insufficient reaction time. It is an unclear phenomenon from a thermodynamic standpoint because the totally hydrogenated **CH-ane** is at least 75 kJ*$mol^{-1}$ more stable as compared to **CH-ene** in terms of the Gibbs free energy [11,50]. But it should be not ruled out the peculiar reaction condition. First, under WGS reaction conditions, where **CH-ene** is saturated *via* hydrogen *in situ* generated from CO and $H_2O$, the low yield of **CH-ane** may be caused by the lack of hydrogen within insufficient surface coverage. This may be due to (i) the $H_2O$ is not almost converted at lower temperatures and reaction time or (ii) because of mass transfer constraints under biphasic conditions, where the hydrogenation reaction rate is determined by the diffusion of hydrogen through the water layer. Supposedly, hydrogen mass transfer is negligible, because the WGS reaction and hydrogenation occurred over the neighboring active sites. Meanwhile, for the water-rich media, decreasing the temperature leads to a lower rate of water transformation through a WGS reaction. Therefore, at a short reaction time, the stagnant water layer may be formed. This layer surrounds the catalyst species inhibiting the **CH-ene** sorption-desorption due to its low solubility in water. It leads to alkylation of **PHE** with **CH-ene**, adsorbed on neighboring active centers (Scheme 2). Note that this alkylation requires the protonation of **CH-ene**, which also indicates the acid function of the catalysts [51]. When the content of **CH-ene** increasing with time, the solubility of **CH-ene** in water may also increase. It results from the diffusion gradient favoring **CH-ene** migration into the aqueous phase, which prevents its hydrogenation to **CH-ane** [12]. The second reason is competitive adsorption: the **PHE**-rich water layer surrounding the catalyst species favors **CH-ene** desorption. When **CH-ene** is desorbing, the water layer disfavors its adsorption over active sites and further hydrogenation to **CH-ane**. At lower temperatures and short reaction times, the hydrogen surface coverage becomes predominant for **CH-ene** hydrogenation to **CH-ane**, because it renders the catalyst surface hydrophobic and protects the active component from water layer formation. On the contrary, when low water containing, at higher temperatures, the hydrogen coverage does not significantly affect the selectivity towards **CH-ene** due to its fast desorption from catalyst active sites. Therefore, as the water content decreases during WGS reaction with time or temperature, the fast **CH-ene** desorption leads to the selectivity towards **CH-ene** increases followed by decreasing with temperature, whereas the selectivity to **CH-ane** and hydrocarbons increases (Scheme 2).

Due to Ni-containing sulfide catalysts having a greater amount of metallic edges and therefore higher hydrogenation activity, they promote the flat sorption of aromatic rings [42,43]. As we proposed, the reaction pathway includes the flat sorption of **GUA** aromatic ring and its coordination by oxygen atom from methoxy group over sulfur vacancies (CUS – coordinatively unsaturated sites) formed through the elimination

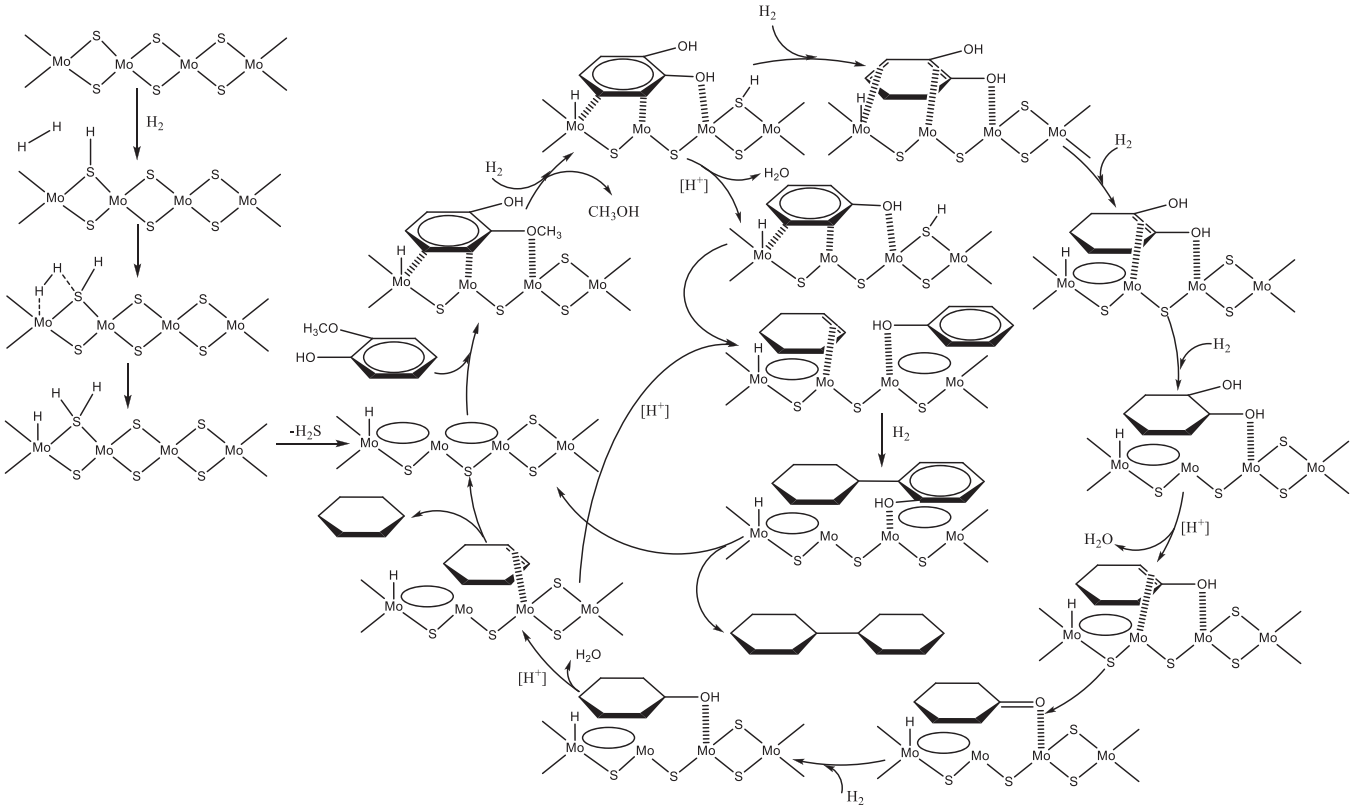


**Scheme 3.** Mechanism of the GUA transformation over $MoS_2$-based unsupported catalyst.

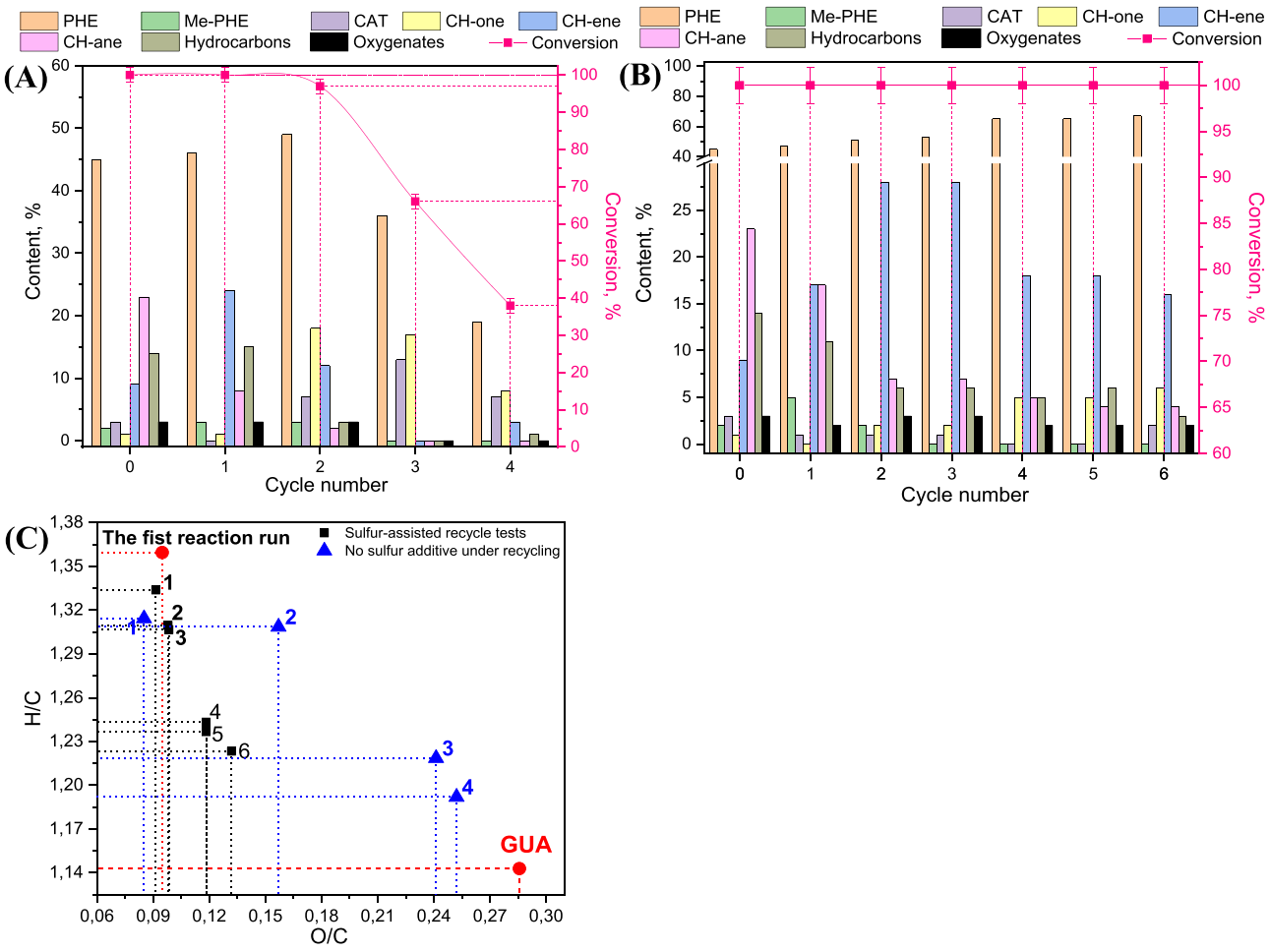


**Fig. 6.** (A) Sulfur-assisted recycling tests and (B) those conducted without sulfur additive (excepted the first reaction run) for Ni-Mo sulfide catalyst from oil-soluble metal precursors in GUA transformation under WGS reaction conditions; (C) Van-Crevelen diagram for products of GUA hydrodeoxygenation under recycling. *Reaction conditions:* ω(Mo) = 0.10 wt%, ω(S) = 1.25 wt%, Ni:Mo= 1:3 (mol/mol), ω($H_2O$) = 20 wt%, p(CO) = 5 MPa (at 25 °C), CO:$H_2O$ = 1.8 (mol/mol), T = 380 °C, t = 6 h.

of $H_2S$ from the Mo-edge of $MoS_2$ slabs as shown on Scheme 3. It is reasonable to conclude, that this type of adsorption requires at least two neighboring CUS. Due to the lowest C-O bond energy for $C_{Ar}O - CH_3$ (247 kJ $mol^{-1}$) as compared to that for $C_{Ar} - OH$ and $C_{Ar} - OCH_3$ (414 kJ $mol^{-1}$ and 356 kJ $mol^{-1}$, respectively) [50], the **GUA** transformation starts from demethylation resulted in catechol. Following this, total hydrogenation of aromatic ring occurred forming cyclohexane diol, which undergoes dehydration to cyclohexenol rapidly transformed to the corresponding ketone through ketone/enol isomerization. **CH-one** is hydrogenated to **CH-ol**, followed by dehydration to **CH-ene**, afterward the vacancies are regenerated by **CH-ane** elimination. If the hydrogen generated through a WGS reaction is not enough or the acid reaction media, the **CH-ene** may interact with **PHE** adsorbed on neighboring sites. It results in the formation of oxygenated compounds like bicyclohexanol or phenylcyclohexanol, followed by their saturation with hydrogen and water elimination, yielded bicycloalkane or phenyl cyclohexane. Note that the content of bicyclic components increases with sulfur adding because it reduces the number of active sites available for **CH-ene** hydrogenation. Moreover, as reported, sulfur additives suppress **PHE** hydrogenation and dehydration reactivity.

### 3.7. Recycling tests and reusability

Since the active component is too sensitive to water and deactivates when lacking hydrogen sulfide, we have evaluated the stability of catalysts *in situ* formed during the first reaction run when no sulfur was added under recycling and for sulfur-assisted recycling tests (Fig. 6). In typical recycling tests, after the first reaction run, when decomposing of oil-soluble metal oxide precursors and sulfidation, the reactor was cooled down, depressurized, and disassembled. The liquid products were separated without catalyst removal from the reactor. Afterward, the catalyst was reused in hydroconversion of GUA under WGS reaction conditions many times without pre-regeneration. For the sulfur-assisted recycling tests, elemental sulfur was added before each cycle. The reusability tests were performed at 380 °C for 6 h under 5 MPa CO pressure and water content of 20 wt%. As was expected, when no sulfur additive is under recycling, the GUA conversion decreases precipitously to 38% by the 4th reaction run (Fig. 6**A**). The deactivation of catalysts causes decreasing in hydrocarbon products like **CH-ene**, **CH-ane**, and bicyclic PHE-derived alkylates, whereas the content of O-containing compounds including **CAT** and **CH-one** increases. Therefore, the H/C ratio decreases with that increasing for O/C under recycling (Fig. 6**C**). As for the sulfur-assisted recycling tests, the GUA conversion was maintained at > 99% for 6 reaction runs (Fig. 6**B**). Meanwhile, the selectivity toward **CH-ane** decreases with cycle number, and by the 6th reaction run, it is not higher than 5%. As opposed to the recycling tests, when no sulfur was added starting from the 2nd run, the sulfur assisting favors *in situ* catalyst regeneration, which leads to the enhanced hydrogenation performance. It is proved by the high content of **CH-ene** and hydrocarbons in products. Despite this, a slight decrease in activity was observed: the yield of **CH-one** and **PHE** increases up to 6% and 67%, respectively, by the 6th cycle, whereas selectivity to **CH-ene** and **CH-**

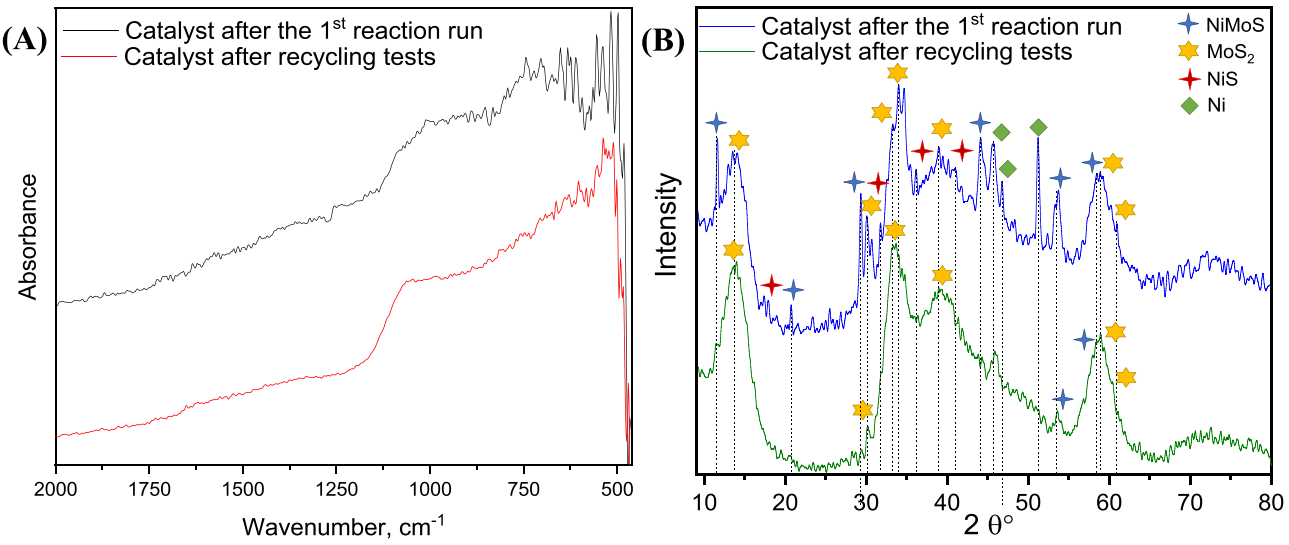


**Fig. 7.** (A) The FT-IR spectrum and (B) XRD pattern for Ni-Mo catalyst formed *in situ* from oil-soluble precursors under WGS reaction conditions during HDO of GUA after the 1st reaction run and after sulfur-assisted recycling tests. *Reaction conditions:* ω(Mo) = 0.10 wt%., Ni:Mo= 1:3 (mol/mol), ω(S) = 1.25 wt%, ω($H_2O$) = 20 wt %, p(CO) = 5 MPa (at 25 ℃), CO:$H_2O$ = 1.8 (mol/mol), T = 380 °C, t = 6 h.

**ane** decreases to 16% and 4%, respectively. Note, that starting from the 3rd reaction run no difference in the GUA conversion and product distribution was observed, and for 4–6 recycles H/C and O/C ratios are close (Fig. 6**C**). Interestingly, by the 2nd cycle, the content of **Me-PHE** and **PHE** alkylation with CH-ene (*i.e.* hydrocarbons and oxygenates) decreases and maintains almost constant. Supposedly, it is caused by a decreased amount of acid sites needed for CH-ene protonation during PHE alkylation.(C).

### 3.8. Catalyst active phase evolution under recycling

To investigate the evolution of active phase species during sulfur-assisted HDO of GUA, we separated the catalyst after the 1st reaction run, during that *in situ* formation of sulfide species occurred at 380 ℃ for 6 h, and that one after 6 cycles, when it was reused under the same reaction conditions. The catalysts were filtered, washed with toluene, and dried in an inert atmosphere. The composition of the catalysts was studied by XRD, IR spectroscopy, TEM, EDX elemental mapping, and XPS techniques.

The IR spectra are poorly resolved due to the complexity of the active phase composition, and the bands for components close resulted in peaks overlapping (Fig. 7**A**). The samples contain octahedral $Ni^{2+}$species, what has been proven by the bands around 500 − 700 $cm^{-1}$. It may overlap with strong absorption bands of $Mo^{6+}$ [52]. The bands around 650 − 670 $cm^{-1}$ could be related to the stretching vibrations of Mo-O-Mo, and the absorbance peak at 660 $cm^{-1}$ indicates the S–H bending band, resulting from $H_2$ dissociative adsorption on $MoS_2$, as well as characterize the bending vibration of $S_xO_y$ species [53]. The bands at 1402 − 1045, 1150, 1080, 660 $cm^{-1}$ corresponded to the $MoS_2$ phase, whereas no signal at 1287 $cm^{-1}$ was observed, showing the lack of Ni in oxide species [53]. Despite the active component forms *in situ* in the water-in-oil emulsions, containing toluene and guaiacol, no bands at 1612 − 1620 $cm^{-1}$ assigned to C= C deformation vibrations or C–C/C = O stretching modes of aromatics or carbonyl compounds were detected. According to the FT-IR data, the catalysts composition slightly differs. For the sample after the 1st reaction run the broad peak with individual signals at the region of 600–750 $cm^{-1}$ indicates the higher content of Ni and Mo compounds, whereas for the analog after recycling tests, the relative intensity decreases. The absorbance peak at the region of 985–1130 $cm^{-1}$ could be assigned to the stretching and bending S–O vibrations [53], and thus its relative intensity increases for the catalysts after the six reaction run due to sulfide surface oxidation. It is also proved by decreasing the absorbance peak at 660 $cm^{-1}$, which could be attributed to the thiosulphate $S_2O_3^{2-}$ ion [53]. The absorbance at 940 $cm^{-1}$ reveals the Mo═O bond in oxysulfide or sulfate species formed through the oxidation of air-contacting $MoS_2$ surface [53]. It was reported that the band at 940 $cm^{-1}$ could be caused by the adsorbed water, whereas weakly adsorbing CO results in a band at 960 $cm^{-1}$ [53]. The oxidized state of the active species for the samples after recycling is proved by the band at 1010–995 $cm^{-1}$, which corresponds to the terminal Mo═O vibrations, where Mo is more likely in a higher oxidation state (6 +).

According to XRD data, the catalysts contain Ni and Mo components (Fig. 7**B**). The XRD patterns are typical for unsupported bimetallic sulfide catalysts. The peak at 2θ ≈ 14° ascribing to the (002) basal planes (according to ICSD powder database standard files, ICSD#601,647) is broadened, indicating poor crystallinity and a low stacking degree of hexagonal $MoS_2$. The increase of interlayer space from 6.15 to 6.30 Å is proved by a slightly shifting reflex to a lower-angle range (13.7–13.9°, hkl = 101) [54]. It is caused by the decrease in coplanarity of $MoS_2$ planes due to incorporating the organic molecules of solvent or substrate because the formation of active components occurs *in situ* [54]. The second reason is the incorporation of Ni atoms yielded NiMoS phase, which is also proved by the reflexes at 29.3° (hkl = 012), 43.9° (hkl = 311), 53.6° (hkl = 223), and 58.3° (hkl = 413) (ICSD#62,183). The intensity of these peaks decreases for the catalyst after recycling tests, indicating the lower NiMoS phase content. For both catalysts, separate Ni and Mo sulfides were detected. The reflexes at 2θ = 14.1° (hkl = 002), 33.3° (hkl = 101), 39.1° (hkl = 103) and 59.2° (hkl = 110) are assigned to the $MoS_2$ (ICSD#601,647), whereas peaks with 2θ = 17.7° (hkl = 110), 30.9° (hkl = 101), 35.1° (hkl = 300), and 41.8° (hkl = 110) are characteristic for NiS (ICSD#151,602). The weak peak at 2θ = 54.3° may correspond to the $Ni_3S_4$ phase (ICSD#601828). Aside from the catalyst after recycling tests, the XRD pattern of the catalyst separated after the 1st reaction run reveals the metallic Ni formation (reflexes at 2θ =45.7 (hkl = 111) and 51.3 (hkl = 200), ICSD#43397). The relative intensity of the 14.1° (hkl = 002) and 33.3° (hkl = 100) peaks allows for concluding the $MoS_2$ slabs have structural defects, which were also observed in TEM images.

The typical multilayer $MoS_2$ black fringes with an interlayer distance of 6.3 ± 0.1 Å were observed in TEM images (Fig. 8**A-C**). As depicted on TEM micrographs, the $MoS_2$ planes are highly stacked along the (001) direction, but they are slightly disordered [9]. The non-bended straight lattice fringes with interplanar space of 2.9 ± 0.1 Å and 4.8 ± 0.1 Å

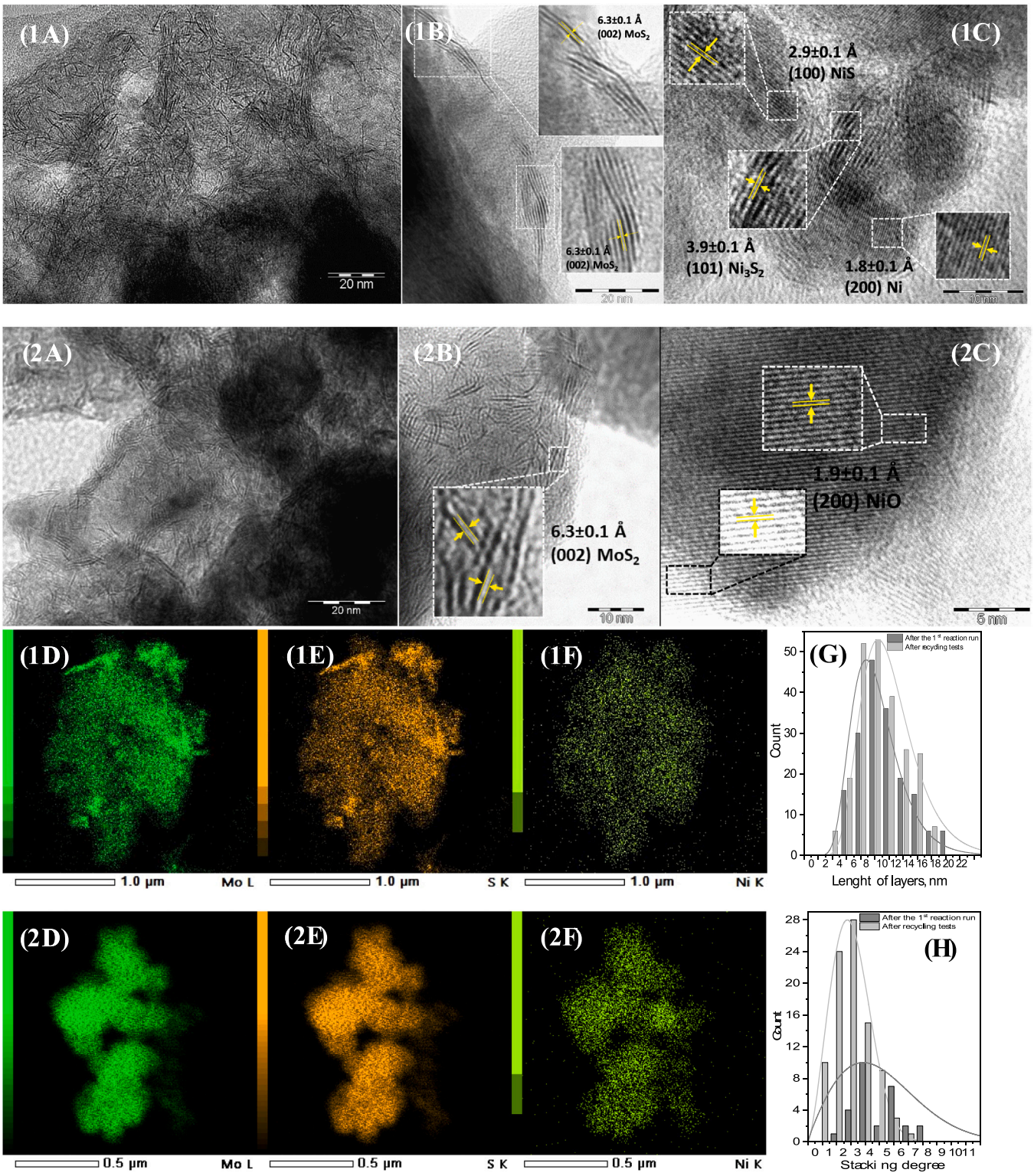


**Fig. 8.** (A-C) TEM images, (D-F) EDX mapping, (G) slab length distribution, and (H) slab stacking degree obtained from TEM for Ni-Mo catalysts formed *in situ* from oil-soluble precursors under WGS reaction conditions (1) after the 1st reaction run and (2) after recycling tests in the hydrogenation of guaiacol.

were ascribed to NiS (100) and NiS (110) phase, respectively [55]. $Ni_3S_2$ (101) with 3.9 ± 0.1 Å space between the black threads were observed on TEM images [56]. As opposed to catalysts after recycling tests, separated after the 1st reaction run counterpart contains the Ni (200) with 1.8 ± 0.1 Å interlayer distance [57], which is in full accordance with XRD data. Meanwhile, TEM images for the sample after recycling tests reveal NiO (200) elongated straight black threads [57]. The slab length distribution and slab stacking degree were obtained by the handling of nearly 300 stacks from different zones of the representative TEM pictures. The histograms were approximated by a Weibull function. According to the slab length distribution, recycling tests lead to elongation of the sulfide particles, whereas the proportion of stacks decreases (Fig. 8**G, H**). EDX elemental maps (Fig. 8**D-F**) reveal Mo, Ni, and S components. The elements are uniformly distributed over the whole

**Table 1**
The characteristics of sulfide species (from XPS and TEM data), composition of sulfide catalysts (from XPS data) and the quantitative XPS analysis of the Mo $3d_{5/2}$, Ni $2p_{3/2}$, and S $2p_{3/2}$ core levels.

| | | Characteristics of active phase species | | | | |
|---|---|---|---|---|---|---|
| Sample | $D$[a] | $\omega NiMoS$, wt%[b] | $\omega NiS_x$, wt%[c] | $\omega MoS_2$,wt%[d] | $p\ (Ni/Mo)_s$[e] | $p\ (Ni/Mo)_e$[f] |
| 1 * | 0.12 | 2.3 | 1.4 | 33.8 | 0.11 | 0.92 |
| 2 * * | 0.10 | 2.7 | – | 15.7 | 0.28 | 2.68 |

| | Surface concentration (at%) and components ratio | | | | |
|---|---|---|---|---|---|
| | Mo *3d* | Ni *2p* | S *2p* | O *1 s* | C *1 s* | Ni/Mo | S/(Ni+Mo) |
| 1 | 4.1 | 1.3 | 12.1 | 29.5 | 53.0 | 0.31 | 2.25 |
| 2 | 2.6 | 1.3 | 12.2 | 34.2 | 49.8 | 0.49 | 3.16 |

| | Mo $3d_{5/2}$, eV (content, %) | | | Ni $2p_{3/2}$, eV (content, %) | | | | S $2p_{3/2}$, eV (content, %) | | |
|---|---|---|---|---|---|---|---|---|---|---|
| | $MoS_2$ | $MoS_xO_y$ | $Mo^{f+}$ | $NiS_x$ | NiMoS | NiO | $Ni^{+2}$ | $S^{b-}$ | $S_2^{b-}$ or $S_{el}$ | $SO_4^{b-}$ |
| 1 | 228.9 (73.6) | 230.3 (7.7) | 232.1 (18.6) | 852.9 (16.0) | 854.1 (26.1) | 856.0 (35.2) | 861.1 (22.7) | 161.6 (72.6) | 163.2 (17.8) | 168.6 (9.6) |
| 2 | 228.7 (45.1) | 230.2 (42.8) | 232.7 (12.0) | – | 853.3 (25.1) | 855.8 (57.2) | 861.1 (17.7) | 161.2 (45.8) | 163.0 (27.0) | 168.6 (27.2) |

* catalyst after the 1st reaction run
* * catalyst after recycling tests
[a] Active phase dispersion (Eq. 5)
[b] The effective Ni content in NiMoS phase (Eq. 6)
[c] The effective Ni content in NiS phase (Eq. 7)
[d] The effective Mo content in $MoS_2$ phase (Eq. 8)
[e] Ni promotion of $MoS_2$ slab (Eq. 9)
[f] The Ni/Mo atomic ratio on the edges (Eq. 10)

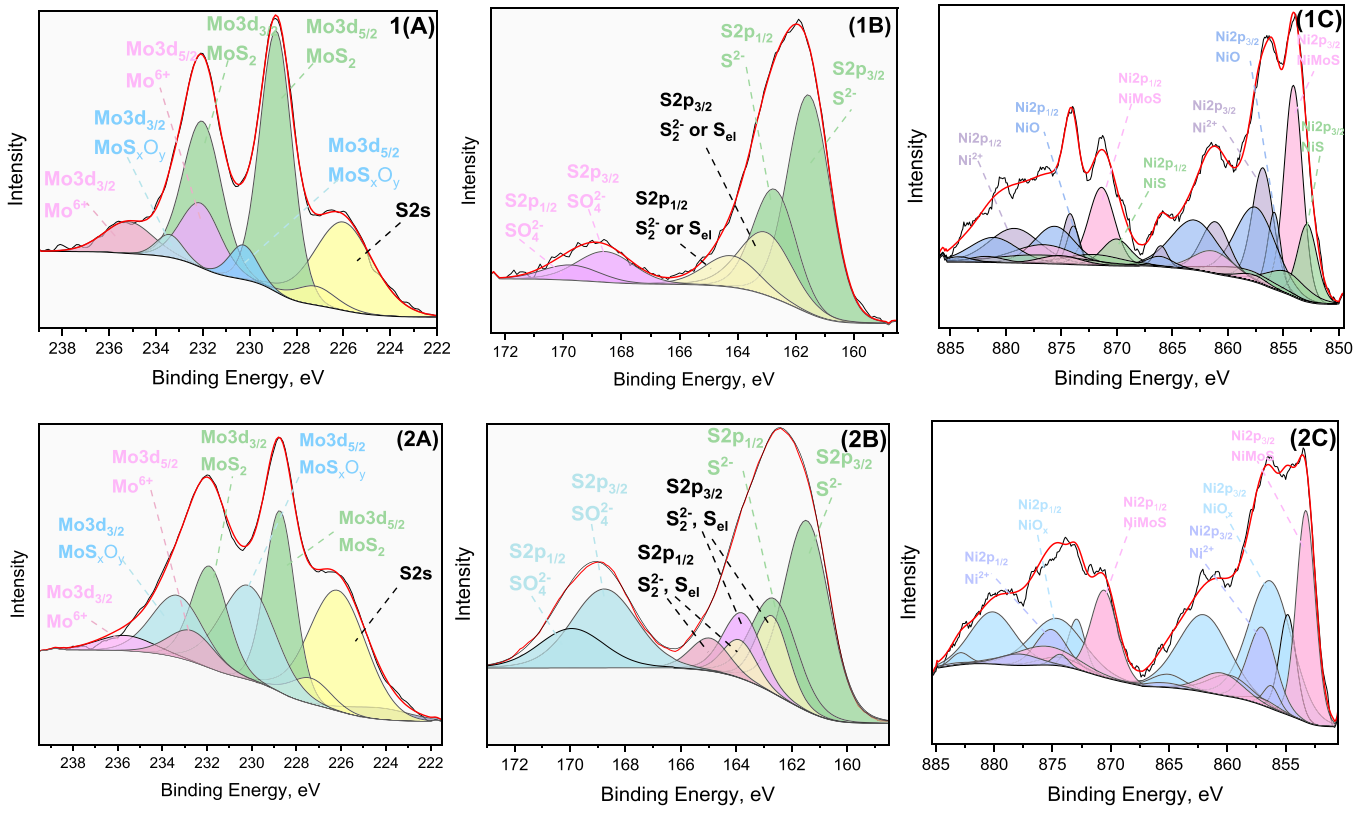


**Fig. 9.** (A) Mo*3d*-*S2 s*, (B) S*2p*, and (C) Ni*2p* core-level spectra for Ni-Mo catalysts formed *in situ* from oil-soluble precursors under WGS reaction conditions (1) after the 1st reaction run and (2) after recycling tests in the hydrogenation of guaiacol (for (C) in green: NiS contribution; in pink: NiMoS phase contribution; in blue: NiO phase contribution; in violet: $Ni^{2+}$ (*i.e.* sulfate or hydroxide) contribution).

area selected. The regions with a higher concentration of Mo are the same as for the S component, showing the formation of the $MoS_2$ phase.

More detailed information about the surface chemical composition was obtained from XPS analysis. The XRS spectra reveal Mo, Ni, and S compounds with calculated Ni/Mo atomic ratios of 0.31 and 0.49 for Ni-Mo catalysts after the 1st reaction run and one after recycling tests, respectively (Table 1). Under recycling, the S/(Ni+Mo) ratio increases, and the composition of active components differs. The Mo*3d*+*S2 s* energy region contains three dublets attributed to Mo in sulfide, oxysulfide, and sulfide or oxide $Mo^{6+}$ species (Fig. 9**A**). As we can see from the data fitted for the Mo*3d*+*S2 s* core level, the relative content of $MoS_2$ decreases to 45.1% for the sample after recycling tests in the hydrogenation of guaiacol, whereas the impact of the $MoS_xO_y$ phase increases up to 42%. The $S2p_{3/2}$ core level spectra reveal the sulfur in sulfide state

decreasing from 72.6% to 45.8%, whereas the content of sulfate increases from 9.6% to 27.2% under recycling (Fig. 9**B**, Table 1). The peaks at 162.5–163 eV are ascribed to the $S_2^{2-}$ sulfur species or elemental sulfur [58], which contains almost 10% higher for catalyst after recycling tests. For Ni*2p* core-level spectra the more significant difference was observed (Fig. 9**C**). As opposed to the catalyst after recycling tests, the Ni$2p_{3/2}$ energy region for the one-time used counterpart contains a characteristic peak at 852.9 eV with corresponding "shake-up" satellites, ascribed to $NiS_x$ species with 16% content [58,59]. The content of the NiMoS phase slightly decreases, whereas the content of NiO reaches 57.2% [60]. For the catalyst after recycling tests, the intensity and relative position of peaks resulted from spin-orbital splitting and lines of the "shake-up" satellite indicate the Ni in oxide state predominantly. Thus, despite the sulfur used as a precursor of sulfiding agent being added under recycling, the active component of the catalyst partially transforms into corresponding oxides. Therefore, the activity in the hydrogenation of guaiacol gradually decreases with cycle number.

According to the calculations of the characteristics and composition of the sulfide species, the sulfur-assisted recycling leads to elongate the average slab length from 10.3 to 11.9 nm, whereas the average slab stacking decreases from 5.1 to 3.0. It results in decreasing a dispersion of active component and therefore the density of the active sites (Table 1). The effective content of Mo in $MoS_2$ phase decreases more than twice, whereas that for Ni in NiMoS phase increases from 2.3 to 2.7. Due to the surface atomic concentration of Ni (according to XPS) and relative content of NiMoS are practically unchanged under recycling, the absolute concentration of Ni in NiMoS species is also retained. As for Mo species, the surface atomic concentration of Mo (according to XPS) and relative content of $MoS_2$ decreases after recycling resulted in lower effective Mo content in $MoS_2$ phase. Summing up, the Ni promotion of $MoS_2$ slab was calculated as a ratio of absolute concentration of Ni in NiMoS species to absolute concentration of Mo in $MoS_2$ phase increases for the sample after recycling. Similarly, the Ni/Mo atomic ratio on the edges increases.

Based on the physicochemical data, we can conclude that due to high dispersibility of oil-soluble precursors, their high-temperature decomposition in the presence of sulfiding agent under water gas shift conditions favors highly stacked 8–9 nm sulfide particles formation. The ligand structure of precursors positively affects on the sulfidation behaviour. The molybdenum hexacarbonyl and nickel naphthenate rapidly decomposes under reaction conditions, followed by nucleation and growth of sulfide particles by exposure to $H_2S$, which forms *in situ* from sulfiding agent precursors. Therefore, the catalysts have a high sulfidation degree and show relevant activity in guaiacol hydrodeoxygenation *via in situ* hydrogen generated through a water gas shift reaction.

## 4. Conclusions

HDO of guaiacol *via in situ* hydrogen produced through WGS reaction over nanosized unsupported NiMo sulfide catalysts from oil-soluble metal precursors with tunable selectivity toward cyclohexene was studied. The active catalytic species were formed *in situ* through the high-temperature decomposition of oil-soluble metal precursors followed by sulfidation in water-in-oil sulfur-containing emulsions. The NiMo unsupported sulfide catalysts were found to provide 100% guaiacol conversion at 320–380 ℃ and 5 MPa CO pressure. The highest H/C ratio was achieved at 340 ℃ and 380 ℃ for 6–8 h, whereas oxygen removal at 380 ℃ for 4 h was almost equal to that at 360 ℃ for 6–8 h.

The Ni additive was found to enhance the hydrogenation activity and the yield of more saturated or dehydrated products increases. The unpromoted Mo-based sulfide catalysts revealed > 99% conversion with lower H/C and higher C/O ratio as compared to those for Ni-containing counterparts. As for the influence of sulfur, which was used as a precursor for hydrogen sulfide (sulfiding agent), at higher temperature it favors dehydration of cyclohexanone or cyclohexanol to cyclohexene. In an account of the transport phenomena considerations and solvent effect based on differences in polarities of products, we examined the influence of water content to adjust selectivity toward cyclohexene in lack of *ex situ* hydrogen. For the water-rich media, at lower temperatures and short reaction times, the hydrogen surface coverage becomes predominant for cyclohexene hydrogenation to cyclohexane, because it renders the catalyst surface hydrophobic and protects the active component from water layer formation. On the contrary, when low water containing, at higher temperatures, the hydrogen coverage does not significantly affect the selectivity towards cyclohexene because of its fast desorption from catalyst active sites. Therefore, as the water content decreases during WGS reaction with time or temperature, the fast cyclohexene desorption leads to increased selectivity, followed by decreasing with temperature. As for the CO pressure, it influences insignificantly compared with water content. It was established that Ni:Mo= 1:3 and sulfur content of 1.2–1.5 wt% favor higher CH-ene selectivity decreases at low temperature and short reaction time under WGS reaction conditions (30–40 wt% water content, CO pressure of 5 MPa).

The catalysts were stable at least 6 cycles in the sulfur-assisted HDO of guaiacol under WGS reaction conditions. The sulfur additive favors *in situ* catalyst regeneration, which leads to enhanced hydrogenation performance. It is proved by the high content of cyclohexene and hydrocarbons in products. The slight decrease in activity expressed as selectivity to cyclohexene and cyclohexane decreasing caused by the evolution of active sulfide species under recycling.

## Funding

The study was financially supported by the Russian Science Foundation (project no. 21–79–10140, https://rscf.ru/project/21–79–10140/).

## CRediT authorship contribution statement

**A.V. Vutolkina:** Supervision, Project administration, Conceptualization, Investigation, Methodology, Writing – review & editing, Writing – original draft, Visualization. **I.G. Baygildin:** Writing – original draft, Visualization, Investigation. **A.P. Glotov:** Writing – original draft, Writing – review & editing, Formal analysis, Resources. **Al.A. Pimerzin:** Writing – review & editing. **A.V. Akopyan:** Writing – review & editing. **A.L. Maksimov:** Conceptualization. **E.A. Karakhanov:** Supervision.

## Declaration of Competing Interest

The authors declare that they have no known competing financial interests or personal relationships that could have appeared to influence the work reported in this paper.

## Acknowledgments

The authors thank Dr. K. Cherednichenko and Dr. A. Stavitskaya for TEM analysis, Dr. D. Svintsitskiy for XPS investigations, Dr. L. Kulikov for GC–GC-TOF MS analysis.

## References

[1] A. Glotov, A. Vutolkina, A. Pimerzin, V. Vinokurov, Y. Lvov, Clay nanotube-metal core/shell catalysts for hydroprocesses, Chem. Soc. Rev. 50 (2021) 9240–9277.
[2] C. Liu, H. Wang, A.M. Karim, J. Sun, Y. Wang, Catalytic fast pyrolysis of lignocellulosic biomass, Chem. Soc. Rev. 43 (2014) 7594–7623.
[3] R.A. Sheldon, Utilisation of biomass for sustainable fuels and chemicals: molecules, methods and metrics, Catal. Today 167 (2011) 3–13.
[4] R. Kumar, V. Strezov, H. Weldekidan, J. He, S. Singh, T. Kan, B. Dastjerdi, Lignocellulose biomass pyrolysis for bio-oil production: a review of biomass pretreatment methods for production of drop-in fuels, Renew. Sustain. Energy Rev. 123 (2020), 109763.
[5] P. Mäki-Arvela, D.Y. Murzin, Hydrodeoxygenation of lignin-derived phenols: from fundamental studies towards industrial applications, Catalysts 7 (2017) 265.

[6] Y. Han, M. Gholizadeh, C.-C. Tran, S. Kaliaguine, C.-Z. Li, M. Olarte, M. Garcia-Perez, Hydrotreatment of pyrolysis bio-oil: a review, Fuel Process. Technol. 195 (2019), 106140.

[7] A.P. Glotov, A.V. Vutolkina, N.A. Vinogradov, A.A. Pimerzin, V.A. Vinokurov, A. A. Pimerzin, Enhanced HDS and HYD activity of sulfide Co-PMo catalyst supported on alumina and structured mesoporous silica composite, Catal. Today 377 (2021) 82–91.

[8] A.A. Pimerzin, A.V. Vutolkina, N.A. Vinogradov, V.A. Vinokurov, Y.M. Lvov, A. P. Glotov, Core-shell catalysts with CoMoS phase embedded in clay nanotubes for dibenzothiophene hydrodesulfurization, Catal. Today (2021).

[9] A.V. Vutolkina, I.G. Baygildin, A.P. Glotov, K.A. Cherednichenko, A.L. Maksimov, E.A. Karakhanov, Dispersed Ni-Mo sulfide catalysts from water-soluble precursors for HDS of BT and DBT *via in situ* produced $H_2$ under Water gas shift conditions, Appl. Catal. B: Environ. 282 (2021), 119616.

[10] E. Laurent, B. Delmon, Influence of water in the deactivation of a sulfided NiMoγ-Al2O3 catalyst during hydrodeoxygenation, J. Catal. 146 (1994) 281–291.

[11] L. Foppa, J. Dupont, Benzene partial hydrogenation: advances and perspectives, Chem. Soc. Rev. 44 (2015) 1886–1897.

[12] C. Zhao, J. He, A.A. Lemonidou, X. Li, J.A. Lercher, Aqueous-phase hydrodeoxygenation of bio-derived phenols to cycloalkanes, J. Catal. 280 (2011) 8–16.

[13] S. Yun, V. Guliants, Hydrogen production over Co-promoted Mo-S water gas shift catalysts supported on $ZrO_2$, Appl. Catal. A: Gen. 590 (2020), 117361.

[14] T. Sasaki, T. Suzuki, M. Takaoka, Y. Akasaka, Performance of a low temperature reactive sulfur-tolerant WGS catalyst using industrial coal gasification gas feed, Int. J. Hydrog. Energy 42 (2017) 2008–2017.

[15] A. Popov, E. Kondratieva, J.-P. Gilson, L. Mariey, A. Travert, F. Maugé, IR study of the interaction of phenol with oxides and sulfided CoMo catalysts for bio-fuel hydrodeoxygenation, Catal. Today 172 (2011) 132–135.

[16] C. Bouvier, Y. Romero, F. Richard, S. Brunet, Effect of $H_2S$ and CO on the transformation of 2-ethylphenol as a model compound of bio-crude over sulfided Mo-based catalysts: propositions of promoted active sites for deoxygenation pathways based on an experimental study, Green. Chem. 13 (2011) 2441–2451.

[17] T. Sasaki, T. Suzuki, H. Iizuka, M. Takaoka, Reaction mechanism analysis for molybdenum-based water-gas shift catalysts, Appl. Catal. A: Gen. 532 (2017) 105–110.

[18] J. Chen, J. Zhang, J. Mi, E.D. Garcia, Y. Cao, L. Jiang, L. Oliviero, F. Maugé, Hydrogen production by water-gas shift reaction over Co-promoted $MoS_2/Al_2O_3$ catalyst: the intrinsic activities of Co-promoted and unprompted sites, Int. J. Hydrog. Energy 43 (2018) 7405–7410.

[19] R.Z. Lee, F.T.T. Ng, Effect of water on HDS of DBT over a dispersed Mo catalyst using in situ generated hydrogen, Catal. Today 116 (2006) 505–511.

[20] R.Z. Lee, M. Zhang, F.T.T. Ng, Hydrodenitrogenation of quinoline over a dispersed molybdenum catalyst using in situ hydrogen, Top. Catal. 37 (2006) 121–127.

[21] A.V. Vutolkina, A.P. Glotov, A.V. Zanina, D.F. Makhmutov, A.L. Maximov, S. V. Egazar'yants, E.A. Karakhanov, Mesoporous Al-HMS and Al-MCM-41 supported Ni-Mo sulfide catalysts for HYD and HDS *via in situ* hydrogen generation through a WGSR, Catal. Today 329 (2019) 156–166.

[22] A. Vutolkina, A. Glotov, I. Baygildin, A. Akopyan, M. Talanova, M. Terenina, A. Maximov, E. Karakhanov, Ni–Mo sulfide nanosized catalysts from water-soluble precursors for hydrogenation of aromatics under water gas shift conditions, Pure Appl. Chem. 92 (2020) 949–966.

[23] P.M. Mortensen, J.D. Grunwaldt, P.A. Jensen, K.G. Knudsen, A.D. Jensen, A review of catalytic upgrading of bio-oil to engine fuels, Appl. Catal. A: Gen. 407 (2011) 1–19.

[24] M.T. Nguyen, N.T. Nguyen, J. Cho, C. Park, S. Park, J. Jung, C.W. Lee, A review on the oil-soluble dispersed catalyst for slurry-phase hydrocracking of heavy oil, J. Ind. Eng. Chem. 43 (2016) 1–12.

[25] K.S. Go, S.H. Lim, Y.K. Kim, E.H. Kwon, N.S. Nho, Characteristics of slurry-phase hydrocracking for vacuum residue with reaction temperature and concentrations of $MoS_2$ dispersed catalysts, Catal. Today 305 (2018) 92–101.

[26] I.A. Sizova, A.B. Kulikov, M.I. Onishchenko, S.I. Serdyukov, A.L. Maksimov, Synthesis of nickel–tungsten sulfide hydrodearomatization catalysts by the decomposition of oil-soluble precursors, Pet. Chem. 56 (2016) 44–50.

[27] K.H. Kang, N.T. Nguyen, D.V. Pham, P.W. Seo, N. Kang, C.W. Lee, M.-C. Chung, C.-H. Kwak, I. Ro, Y.-P. Jeon, S. Park, Ligand structure effect in oil-soluble phosphorus-containing molybdenum precursors for slurry-phase hydrocracking of heavy oil, J. Catal. 402 (2021) 194–207.

[28] Z. Cai, Y. Ma, J. Zhang, W. Wu, Y. Cao, L. Jiang, K. Huang, Tunable ionic liquids as oil-soluble precursors of dispersed catalysts for suspended-bed hydrocracking of heavy residues, Fuel 313 (2022), 122664.

[29] A.V. Vutolkina, D.F. Makhmutov, A.V. Zanina, A.L. Maximov, D.S. Kopitsin, A. P. Glotov, S.V. Egazar'yants, E.A. Karakhanov, Hydroconversion of thiophene derivatives over dispersed Ni–Mo sulfide catalysts, Pet. Chem. 58 (2018) 1227–1232.

[30] C.N. Siewe, F.T.T. Ng, Hydrodesulfurization of cold lake diesel fraction using dispersed catalysts: influence of hydroprocessing medium and sources of H2, Energy Fuels 12 (1998) 598–606.

[31] A.V. Vutolkina, A.P. Glotov, A.L. Maximov, E.A. Karakhanov, Hydroconversion of 2-methylnaphtalene and dibenzothiophene over sulfide catalysts in the presence of water under CO pressure, Russ. Chem. Bull. 69 (2020) 280–288.

[32] E.A. Roldugina, E.R. Naranov, A.L. Maximov, E.A. Karakhanov, Hydrodeoxygenation of guaiacol as a model compound of bio-oil in methanol over mesoporous noble metal catalysts, Appl. Catal. A: Gen. 553 (2018) 24–35.

[33] M.A. Golubeva, E.M. Zakharyan, A.L. Maximov, Transition metal phosphides (Ni, Co, Mo, W) for hydrodeoxygenation of biorefinery products (a review), Pet. Chem. 60 (2020) 1109–1128.

[34] B. Yoosuk, D. Tumnantong, P. Prasassarakich, Amorphous unsupported Ni–Mo sulfide prepared by one step hydrothermal method for phenol hydrodeoxygenation, Fuel 91 (2012) 246–252.

[35] W. Wang, L. Li, S. Tan, K. Wu, G. Zhu, Y. Liu, Y. Xu, Y. Yang, Preparation of NiS2// MoS2 catalysts by two-step hydrothermal method and their enhanced activity for hydrodeoxygenation of p-cresol, Fuel 179 (2016) 1–9.

[36] K. Wu, Y. Liu, W. Wang, Y. Huang, W. Li, Q. Shi, Y. Yang, Preparation of hydrophobic $MoS_2$, $NiS_2$-$MoS_2$ and $CoS_2$-$MoS_2$ for catalytic hydrodeoxygenation of lignin-derived phenols, Mol. Catal. 477 (2019), 110537.

[37] C.-C. Tran, F. Stankovikj, M. Garcia-Perez, S. Kaliaguine, Unsupported transition metal-catalyzed hydrodeoxygenation of guaiacol, Catal. Commun. 101 (2017) 71–76.

[38] Y. Ma, J. Zhang, W. Wu, Z. Cai, Y. Cao, K. Huang, L. Jiang, Trialkylmethylammonium molybdate ionic liquids as novel oil-soluble precursors of dispersed metal catalysts for slurry-phase hydrocracking of heavy oils, Chem. Eng. Sci. 253 (2022), 117516.

[39] S. Kasztelan, H. Toulhoat, J. Grimblot, J.P. Bonnelle, A geometrical model of the active phase of hydrotreating catalysts, Appl. Catal. 13 (1984) 127–159.

[40] H. Topsφe, B.S. Clausen, Importance of Co-Mo-S type structures in hydrodesulfurization, Catal. Rev. 26 (1984) 395–420.

[41] M. Sun, A.E. Nelson, J. Adjaye, Adsorption and dissociation of $H_2$ and $H_2S$ on $MoS_2$ and NiMoS catalysts, Catal. Today 105 (2005) 36–43.

[42] A. Popov, E. Kondratieva, L. Mariey, J.M. Goupil, J. El Fallah, J.-P. Gilson, A. Travert, F. Maugé, Bio-oil hydrodeoxygenation: adsorption of phenolic compounds on sulfided (Co)Mo catalysts, J. Catal. 297 (2013) 176–186.

[43] P.G. Moses, J.J. Mortensen, B.I. Lundqvist, J.K. Nørskov, Density functional study of the adsorption and van der Waals binding of aromatic and conjugated compounds on the basal plane of $MoS_2$, The, J. Chem. Phys. 130 (2009), 104709.

[44] Y. Romero, F. Richard, S. Brunet, Hydrodeoxygenation of 2-ethylphenol as a model compound of bio-crude over sulfided Mo-based catalysts: promoting effect and reaction mechanism, Appl. Catal. B: Environ. 98 (2010) 213–223.

[45] B. Yoosuk, J.H. Kim, C. Song, C. Ngamcharussrivichai, P. Prasassarakich, Highly active $MoS_2$, $CoMoS_2$ and $NiMoS_2$ unsupported catalysts prepared by hydrothermal synthesis for hydrodesulfurization of 4,6-dimethyldibenzothiophene, Catal. Today 130 (2008) 14–23.

[46] I. Gandarias, V.L. Barrio, J. Requies, P.L. Arias, J.F. Cambra, M.B. Güemez, From biomass to fuels: hydrotreating of oxygenated compounds, Int. J. Hydrog. Energy 33 (2008) 3485–3488.

[47] J. Leglise, J. van Gestel, J.C. Duchet, Promotion and inhibition by hydrogen sulfide of thiophene hydrodesulfurisation over a sulfide catalyst, J. Chem. Soc., Chem. Commun. (1994) 611–612.

[48] I.B. Adilina, N. Rinaldi, S.P. Simanungkalit, F. Aulia, F. Oemry, G.B.G. Stenning, I. P. Silverwood, S.F. Parker, Hydrodeoxygenation of Guaiacol as a bio-oil model compound over pillared clay-supported nickel–molybdenum catalysts, J. Phys. Chem. C. 123 (2019) 21429–21439.

[49] X. Zhang, Q. Zhang, T. Wang, L. Ma, Y. Yu, L. Chen, Hydrodeoxygenation of lignin-derived phenolic compounds to hydrocarbons over $Ni/SiO_2$–$ZrO_2$ catalysts, Bioresour. Technol. 134 (2013) 73–80.

[50] N.K.G. Silva, R.M. Ribas, R.S. Monteiro, M.A.D.S. Barrozo, R.R. Soares, Thermodynamic equilibrium analysis of the vapor phase hydrodeoxygenation of guaiacol, Renew. Energy 147 (2020) 947–956.

[51] E.-M. Ryymin, M.L. Honkela, T.-R. Viljava, A.O.I. Krause, Competitive reactions and mechanisms in the simultaneous HDO of phenol and methyl heptanoate over sulphided $NiMo/\gamma$-$Al_2O_3$, Appl. Catal. A: Gen. 389 (2010) 114–121.

[52] H. Liu, C. Yin, X. Li, Y. Chai, Y. Li, C. Liu, Effect of NiMo phases on the hydrodesulfurization activities of dibenzothiophene, Catal. Today 282 (2017) 222–229.

[53] A.A. Tsyganenko, F. Can, A. Travert, F. Maugé, FTIR study of unsupported molybdenum sulfide—in situ synthesis and surface properties characterization, Appl. Catal. A: Gen. 268 (2004) 189–197.

[54] B.S. Zhang, Y.J. Yi, W. Zhang, C.H. Liang, D.S. Su, Electron microscopy investigation of the microstructure of unsupported Ni–Mo–W sulfide, Mater. Charact. 62 (2011) 684–690.

[55] Y. Zhong, J. Yuan, J. Wen, X. Li, Y. Xu, W. Liu, S. Zhang, Y. Fang, Earth-abundant NiS Co-catalysts modified metal-free mpg-$C_3N_4$/CNTs nanocomposites for highly efficient visible-light photocatalytic $H_2$ evolution, Dalton Trans. (Camb., Engl.: 2003) 44 (2015).

[56] S. Deng, K. Zhang, D. Xie, Y. Zhang, Y. Zhang, Y. Wang, J. Wu, X. Wang, H. Fan, X. Xia, J. Tu, High-index-faceted $Ni_3S_2$ branch arrays as bifunctional electrocatalysts for efficient water splitting, Nano-Micro Lett. 11 (2019) 12.

[57] J. Li, P. Li, J. Li, Z. Tian, F. Yu, Highly-dispersed Ni-NiO nanoparticles anchored on an $SiO_2$ support for an enhanced CO methanation performance, Catalysts 9 (2019) 506.

[58.] C.D. Wagner, N.I.S.T. X-ray, photoelectron spectroscopy database, NIST Standarad Reference, Database 20 (2000).

[59] A.D. Gandubert, C. Legens, D. Guillaume, S. Rebours, E. Payen, X-ray photoelectron spectroscopy surface quantification of sulfided CoMoP catalysts – relation between activity and promoted sites – part I: influence of the Co/Mo ratio, Oil Gas. Sci. Technol. - Rev. De. l'IFP 62 (2007) 79–89.

[60] D.A. Svintsitskiy, M.K. Lazarev, T.Y. Kardash, E.A. Fedorova, E.M. Slavinskaya, A. I. Boronin, Mixed silver-nickel oxide $AgNiO_2$: probing by CO during XPS study, J. Chem. Phys. 152 (2020), 044707.